



Engineered M2-sEV encapsulated Se-mRh nanoparticles with Fe²⁺ chelating capability inhibit ferroptosis for Alzheimer's disease treatment

Chaonan Jing^{a,b,c,1}, Kezhen Ge^{c,1}, Dehong Yu^{d,1}, Minghao Chao^{e,1}, Yiming Yin^{a,b}, Junjie Li^c, Yufan Liu^c, Guangyu Ma^c, Rongze Tang^c, Silin Du^c, Yingcai Xu^c, Jiangbo Wang^{a,b,*}, Fenglei Gao^{c,*}, Guanqun Zhang^{a,b,*}

^a Department of Neurology, Xuzhou Central Hospital, Xuzhou, Jiangsu, 221002, China

^b Department of Neurology, Xuzhou Clinical School of Xuzhou Medical University, Xuzhou, Jiangsu, 221002, China

^c Jiangsu Key Laboratory of New Drug Research and Clinical Pharmacy, Xuzhou Medical University, Xuzhou, Jiangsu, 221004, China

^d Department of Oncology, The Affiliated Pizhou Hospital of Xuzhou Medical University, Pizhou, Jiangsu, 221399, China

^e Department of Orthopaedic Surgery, Lishui Central Hospital and Fifth Affiliated Hospital of Wenzhou Medical University, Lishui, 323000, Zhejiang, China

ARTICLE INFO

Keywords:

Ferroptosis
Mitochondrial ROS
Inflammation
Neuronal death

ABSTRACT

Abnormal iron deposition and brain immunoinflammation are significant contributors to the pathophysiological consequences of Alzheimer's disease, where in mitochondrial dysfunction plays a crucial role in eliciting cellular inflammatory responses and facilitating iron accumulation. Mitochondrial-targeted therapy emerges as a promising strategy, with the combination of metal ions and polyphenols showing substantial potential for clearing excess iron ions and reshaping the brain microenvironment. However, the use of metal ions or polyphenols in isolation suffers from poor targeting, inadequate metabolic stability, and low bioavailability, which fail to meet clinical requirements. In this study, Se-mesoporous Rh (Se-mRh) was modified with tannic acid (TA) and subsequently encapsulated within M2-sEV to establish a dual-targeting mechanism that leverages exosomal chemotaxis navigation alongside TA-mediated mitochondrial anchoring. This approach aims to reshape the brain microenvironment by inhibiting abnormal iron ion deposition and mitigating associated inflammatory responses while preserving neuronal viability. Simultaneously, we reconstructed the endogenous defense system via Nrf2-mediated signaling pathways, restoring the homeostatic cycle of iron transfer-storage-output while further augmenting cellular antioxidant capacity. This study presents an innovative treatment strategy for Alzheimer's disease and establishes a new paradigm for addressing specific neurological disorders.

1. Introduction

Neurodegenerative diseases, especially Alzheimer's disease (AD), have become a major threat to the health of the elderly [1]. The clinical manifestations of AD are mainly cognitive dysfunction, accompanied by neuropsychiatric symptoms (BPSD) and loss of activities of daily living (ADL) [2]. Pathologically, AD is characterized by the cleavage of amyloid precursor protein (APP) by β -secretase and γ -secretase to produce toxic A β [3]. Although apoptotic mechanisms were suggested early on as possible causes of neuronal loss, clinical studies found that apoptosis inhibitors failed to significantly improve AD [4], suggesting that apoptosis may not be the primary pathogenic mechanism. Recently, siderophore apoptosis has been proposed as a novel mode of cell death,

mainly caused by free iron overload and lipid peroxidation [5]. The pathogenesis of Alzheimer's disease (AD) is highly consistent with the characteristics of ferroptosis, including abnormal brain iron accumulation [6], GSH depletion, and decreased GPX4 activity [7]. This association has been demonstrated in related AD models, such as APP/PS1 [8] transgenic mice, STZ-induced [9] insulin resistance models, and scopolamine-induced [10] cholinergic injury models, all showing ferroptosis to be involved in AD neurodegeneration. Therefore, abnormal activation of ferroptosis pathway may be an important driver of AD progression, and inhibition of ferroptosis may be a potential strategy to control the development of AD.

The inactivation of iron regulatory proteins (IRPs) plays a crucial role in neuronal iron overload [11]. The downregulation of ferroportin 1

* Corresponding authors.

E-mail addresses: wangjiangbo2011@126.com (J. Wang), flgao@xzhmu.edu.cn (F. Gao), zgq18@sina.com (G. Zhang).

¹ These authors contributed equally to this research work.

(FPN1) expression, along with impaired ferritin heavy chain (FTH1) activity [12], results in iron retention and the accumulation of reactive oxygen species (ROS) [13]. Disruption of the labile iron pool (LIP) homeostasis is central to ferroptosis in Alzheimer's disease (AD) [14], where Fe^{2+} catalyzes the generation of hydroxyl radicals ($\cdot\text{OH}$) [15] through the Fenton reaction, initiating a cascade of lipid peroxidation (LPO) [16]. Additionally, imbalances in mitochondrial iron pool (mLIP) homeostasis exacerbate neurodegeneration by disrupting the electron transport chain [17]. This occurs through the production of mitochondrial ROS (mROS) [18] and activation of the mitochondrial permeability transition pore (mPTP) [19], further promoting ferroptosis [20]. In recent years, the use of metal nanoparticles, hydrogels, and natural polyphenolic compounds in disease treatment has garnered significant attention [21]. However, these strategies face considerable challenges in treating AD [22]. Despite their functional diversity, these materials have limited bioavailability at lesion sites due to their systemic distribution [23]. While nanoparticles modified with positively charged lipophilic groups can enhance mitochondrial targeting, their positive surface charge increases the risk of nonspecific deposition in the bloodstream, as observed with compounds such as triphenylphosphine (TPP) [24], Szeto-Schiller (SS-31) [25], guanidine [26], and biguanide. Such deposition can provoke inflammatory responses and hinder blood-brain barrier (BBB) penetration [27]. To address these challenges, tannic acid (TA), a natural polyphenolic derivative, offers distinct advantages [28]. Its negative charge prevents blood compatibility issues, and it can achieve targeted delivery by binding to the mitochondrial outer membrane protein [29]. In this study, M2 microglia extracellular vesicles were employed as carriers. These exosomes, decorated with chemokines such as CCL2 [30], can actively recognize inflammatory signals, facilitating a dual-targeting mechanism of "exosome chemotactic navigation" and "TA mitochondrial anchoring". This enhances drug delivery while minimizing unwanted deposition in the brain [31]. Furthermore, selenium enhances peroxide removal via the GPX4/GSH system and chelates excess iron to prevent the Fenton reaction [32]. Rhodium nanoclusters, a novel nanozyme, mimic the natural antioxidant enzyme system by exhibiting dual catalytic activities-superoxide dismutase (SOD) and catalase (CAT) [33]. This unique dual-enzyme property allows for efficient scavenging of reactive oxygen/nitrogen species (RONS), particularly superoxide anions. Together, this combined strategy improves therapeutic precision and bioavailability through synergistic spatial positioning and molecular recognition.

In this study, we developed a novel multimodal composite nanomedicine (SRTM2), which comprises tannic acid, selenite, mesoporous rhodium (mRh), and M2-type microglial extracellular vesicles (M2-sEV). By leveraging the targeted delivery capabilities of M2-sEV, the modification potential of TA, and the catalytic properties of the mRh-selenite complex, the nanomedicine exhibits a triple synergistic therapeutic effect. Specifically, it (1) efficiently eliminates mitochondrial reactive oxygen species (mROS) via a targeted catalytic cascade, (2) selectively chelates Fe^{2+} ions in the pathological microenvironment, and (3) utilizes the natural metabolic pathways of M2-sEV to promote nanoparticle efflux, thereby reducing the risk of nanoparticle accumulation in the brain [34]. *In vitro* studies demonstrated that SRTM2 nanoparticles effectively mitigate RSL3-induced neuronal ferroptosis by upregulating glutathione peroxidase 4 (GPX4) expression, activating the Nrf2 antioxidant signaling pathway, and concurrently reducing reactive oxygen species (ROS) and iron ion accumulation, thereby significantly alleviating neuronal injury [35]. *In vivo* experiments further revealed that SRTM2 nanoparticles exhibit remarkable blood-brain barrier penetration, precisely target AD lesions, and possess unique metabolic regulatory properties that facilitate the rapid clearance of nanoparticles upon completion of their therapeutic action. This study integrates five functional modules: targeted delivery, multimodal antioxidant activity, metal ion homeostasis regulation, inflammatory microenvironment remodeling, and intelligent metabolism, to address key challenges in Alzheimer's disease (AD) treatment. These challenges include low blood-

brain barrier penetration efficiency, the difficulty of coordinating multiple pathological pathways, and the insufficient biological safety of nanomaterials. This multi-dimensional, synergistic therapeutic strategy not only provides a novel paradigm for designing nanodrugs for neurodegenerative diseases but also holds significant clinical translational potential.

2. Materials and methods

2.1. *In vitro* cytotoxicity

HT22 and BV2 cells were seeded in 96-well plates at a density of 5×10^3 cells per well and incubated overnight. Then, different concentrations of SRTM2 NPs were added to HT22 and BV2 cells and incubated for 24 h. After incubation, the Wells were washed three times with PBS, and 100 μL of CCK-8 (KGA9305-1000 KeyGen, China) working solution (90 μL of medium +10 μL of CCK-8) was added to each well. Incubate at 37°C for 2 h and measure the absorbance of the supernatant at 450 nm.

2.2. Cell uptake experiment

Cells (5×10^5) were seeded into each confocal dish. DiD-labeled M2-Sev was then added to the HT22 cell culture medium. To label mitochondria, the cells were treated with Mito-Tracker Green and incubated for 30 min. Subsequently, the cell nuclei were stained with DAPI (Key-GEN, China) for 6 min. Finally, the cellular uptake of M2-Sev was detected using confocal laser scanning microscopy (Leica STELLARIS 5, Germany).

2.3. JC-1 quantitative analysis

BV2 cells (3×10^5) were resuspended in 0.5 mL of medium, and 0.5 mL of JC-1 staining working solution (Beyotime, China) was added. After mixing, the cells were incubated at 37°C for 20 min in the dark. Following incubation, the cells were centrifuged at $600 \times g$ and 4°C for 3 min, and the supernatant was discarded. The pellet was then washed twice with JC-1 staining buffer and resuspended. Finally, JC-1 fluorescence was measured by flow cytometry.

2.4. Live/dead staining

The experimental group includes the control group, the SR group, the SRT group and the SRTM2 group. After HT22 cells were cultured in 6-well plates for 12 h, they were treated with different materials and stained with Calcein-AM/PI (5 μM , 1 mL) for 30 min to evaluate cell viability. The ratio of living cells (green) to dead cells (red) was observed under an inverted fluorescence microscope.

2.5. Performance evaluation of chelating Fe^{2+} by SRTM2 NPs

The Fe^{2+} chelating ability of SRTM2 NPs was detected using the iron ion content determination kit of Beijing Boaosan Biotechnology Co., LTD. In short, the solution containing FeSO_4 (100 μM) was incubated with SRTM2 of different concentrations at room temperature for 1 h. Then, the concentration of Fe^{2+} was determined by measuring the absorbance of the blue tripyridine-triazine- Fe^{2+} complex at 600 nm by ultraviolet-visible spectroscopy ($n = 3$ for each group). Different concentrations of SRTM2 were incubated with the Fe^{3+} standard solution (50 mM FAC) at room temperature for 4 h to determine its chelating ability for Fe^{3+} . The concentration of Fe^{3+} in each mixture was calculated by determining the absorbance of 2, 2'-bipyridine- Fe^{3+} complex at 520 nm by ultraviolet-visible spectroscopy ($n = 3$ for each group).

2.6. Apoptosis detection

HT22 cells were inoculated in 6-well plates and incubated for 12 h to

ensure cell adhesion. Add A β and incubate with PBS, SR, SRT and SRTM2 for 12 h. Discard the supernatant, wash the cells with PBS, treat the cells with the Annexin V FITC/PI apoptosis detection kit, and analyze the fluorescence signals of different groups by flow cytometry.

2.7. Determination of GSH, MDA and SOD in cells

HT22 cells were sown overnight in 6-well plates and treated with different groups. Subsequently, the GSH level was detected using the GSH and GSSG assay kits, and the contents of malondialdehyde (MDA) and superoxide dismutase (SOD) were detected using the MDA and SOD content assay kits.

2.8. Flow cytometry analysis

After co-culture with different formulations, the well-growing cells were digested with trypsin (without EDTA), and the adherent cells were gently blown off. Subsequently, centrifuge at 800 rpm for 5 min to collect the cells, resuspend them in PBS and count them. The resuspended cells (1×10^6) were rinsed twice with PBS pre-cooled to 4 °C. Subsequently, 100 μ L of the antibody staining solution was added, followed by gentle shaking. The cells were incubated in a dark room at room temperature for 30 min and finally detected by flow cytometry.

2.9. Western blotting analysis

On ice, the prefrontal cortex and hippocampal tissues of mice were promptly isolated and removed. The sample was immediately homogenized in a cocktail buffer of cryoprotease inhibitor containing RIPA. To ensure complete rupture of the tissue, homogenize the tissue and then place it at 4 °C for 30 min. After centrifugation at 12,000 rpm for 15 min at 4 °C, the supernatant was extracted from the lysate. The protein concentration was determined using the BCA protein concentration determination kit. The protein ran on an electrophoresis column at 90 V for 80 min and then moved onto a PVDF membrane. Seal the film with 5% skimmed milk for 2 h to prevent non-specific binding. Afterwards, the primary antibody was added to the membrane and incubated overnight at 4 °C. The next day, clean the membrane with TBST. After cleaning with TBST three times, incubate with the secondary antibody for 40 min. A gel image system. 4.00 is used for observing the blotting membrane.

2.10. Reactive oxygen species scavenging experiment

The antioxidant potential of SRTM2 NPs was initially detected by two methods: the 2, 2'-nitrogen-bis (3-ethylbenzothiazole-6-sulfonic acid) method and the DPPH method. In the ABTS clearance experiment, samples containing different concentrations of SRTM2 were introduced into the ABTS working solution (5 mM, prepared with PBS). Then store the resulting mixture in a dark environment at room temperature for 10 min. Then, the absorbance at 415 nm was measured using a UV-Vis spectrophotometer, with three measurements for each group. In the DPPH experiment, 3 mL of DPPH ethanol solution (0.1 mM) was freshly prepared. Subsequently, different concentrations of SRTM2 were added to the DPPH solution, with each concentration being 100 μ g/mL. The changes in absorbance at 517 nm were monitored using a UV-Vis spectrophotometer, and these measurements were conducted three times for each group. The ability of SRTM2 NPs to eliminate H₂O₂ was evaluated by colorimetry. Simply put, incubate the H₂O₂ solution (1 mM) with SRTM2 at room temperature for 1 h. Then, by observing the absorption of hydrogen peroxide - titanium at 410 nm, the concentration of H₂O₂ was determined by ultraviolet-visible spectroscopy ($n = 3$). Then, the degradation of SRTM2 in H₂O₂ solutions of different concentrations was monitored by ultraviolet-visible spectroscopy. The mixture should be stored dark at room temperature for 24 h. After the incubation period, the absorption spectra of the mixture were captured

using a UV-Vis spectrophotometer.

2.11. In vitro blood-brain barrier transport analysis

The in vitro blood-brain barrier model was established using Transwell plates. Mouse brain microvascular endothelial cells were sown in the parietal chamber of Transwell. Then HT22 cells were injected into the bottom compartment. Change the culture medium every other day and measure TEER with a TEER meter. These cells have been treated in different ways. Finally, the fluorescence intensity of HT22 cells was evaluated using a laser scanning confocal microscope (excitation wavelength 754 nm).

2.12. In vivo fluorescence imaging

At 30 min, 6, 12, 24, 36 and 48 h after tail vein injection of DiD-labeled SRTM2 in mice, the mice were imaged using the in vivo imaging system (IVIS Lumina S5). The fluorescence imaging results and average radiation intensity were reported brain tissues were taken for 48 h, sliced into 20 μ m histological sections, stained with DAPI, and observed under a fluorescence confocal laser microscope.

2.13. Behavioral assessment

In the OFT, the opening size was 40 \times 40 \times 40 cm, and each mouse was placed in the center of the bottom and moved freely for 5 min. Record the percentage of time and distance of the mice in the inner and outer squares. In the Y-shaped maze test, the three arms were respectively marked as the starting arm, the other arm and the new arm. This process includes training and test experiments. In the training experiment, the new arm was blocked by a baffle, and the mice were placed in the starting arm, allowing them to freely explore the maze for 5 min. After an interval of 1 h, the new arm is opened for the test experiment. The mice were placed in the initial group again and allowed to freely explore the maze for 5 min. The distance, time and number of entries of the new arm were recorded. In the MWM test, a circular water tank with a diameter of 120 cm was filled with water and maintained at 21–24 °C. A platform with a diameter of 12 cm is hidden more than 1.5 cm below the water surface [10]. Define the quadrant where the platform is located as the target quadrant. In the navigation orientation experiment, each mouse was placed in water facing the water tank from four quadrants for five days of training. If the mouse does not reach the platform within 60 s, guide it to the platform and stay on it for 30 s. On the 6th day, the fixed platform was moved out of the maze. The mice were placed at the position farthest from the platform and allowed to swim freely for 60 s. Record the escape latency period, the distance and time in the target quadrant, as well as the number of times crossing the platform.

2.14. Perl's Prussian blue staining

After all treatments were completed, brain tissues were collected and fixed in 4% paraformaldehyde solution for 24 h, followed by dehydration in 30% sucrose solution for 48 h, with one solution change during the process. The tissues were then embedded in paraffin and sectioned. Perl's staining solution was added dropwise to the sections and incubated at 37 °C for 20 min. After rinsing three times with distilled water, incubation droplets were added to the sections and incubated for another 20 min at 37 °C. The sections were rinsed three times with distilled water, and enhancement working solution droplets were added to the sections and incubated for 10 min at 37 °C. After rinsing three times with PBS, composite dye was added for staining for 5 min. Finally, the sections were washed, dehydrated, and sealed.

2.15. Detection of intracellular and mitochondrial ROS

The levels of intracellular and mitochondrial reactive oxygen species (ROS) were determined using the DCFH-DA and MitoSOX Red indicators. HT22 cells were exposed to different dispersions (PBS, SR, SRT, SRTM2) for 6 h. After washing with PBS, the cells were cultured in serum-free medium containing DCFH-DA (10 μ M, 1 mL) and MitoSOX Red (10 μ M, 1 mL) for 30 min, and then imaged using confocal laser scanning microscopy (CLSM) (Leica STELLARIS 5, Germany).

2.16. Statistical analysis

Data are expressed as mean \pm standard deviation. GraphPad 8.0.2 software was used, and the unpaired *t*-test was used for comparison between the two groups. Parametric one-way analysis of variance was used for comparisons of more than two groups. If $p < 0.05$, it is considered statistically significant. To * $p < 0.05$, ** $p < 0.01$, *** $p < 0.001$, **** $p < 0.0001$ for significant standards.

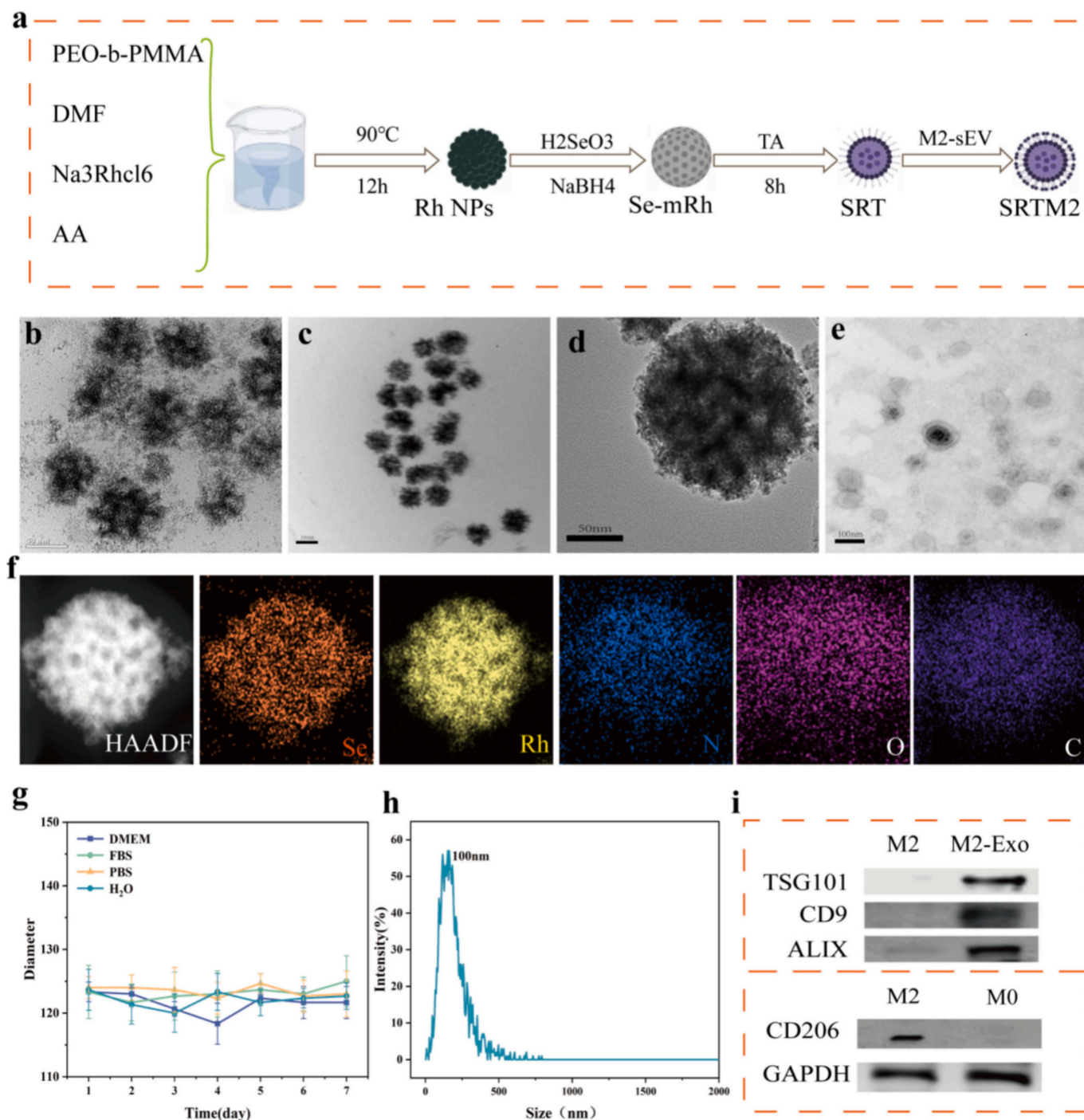


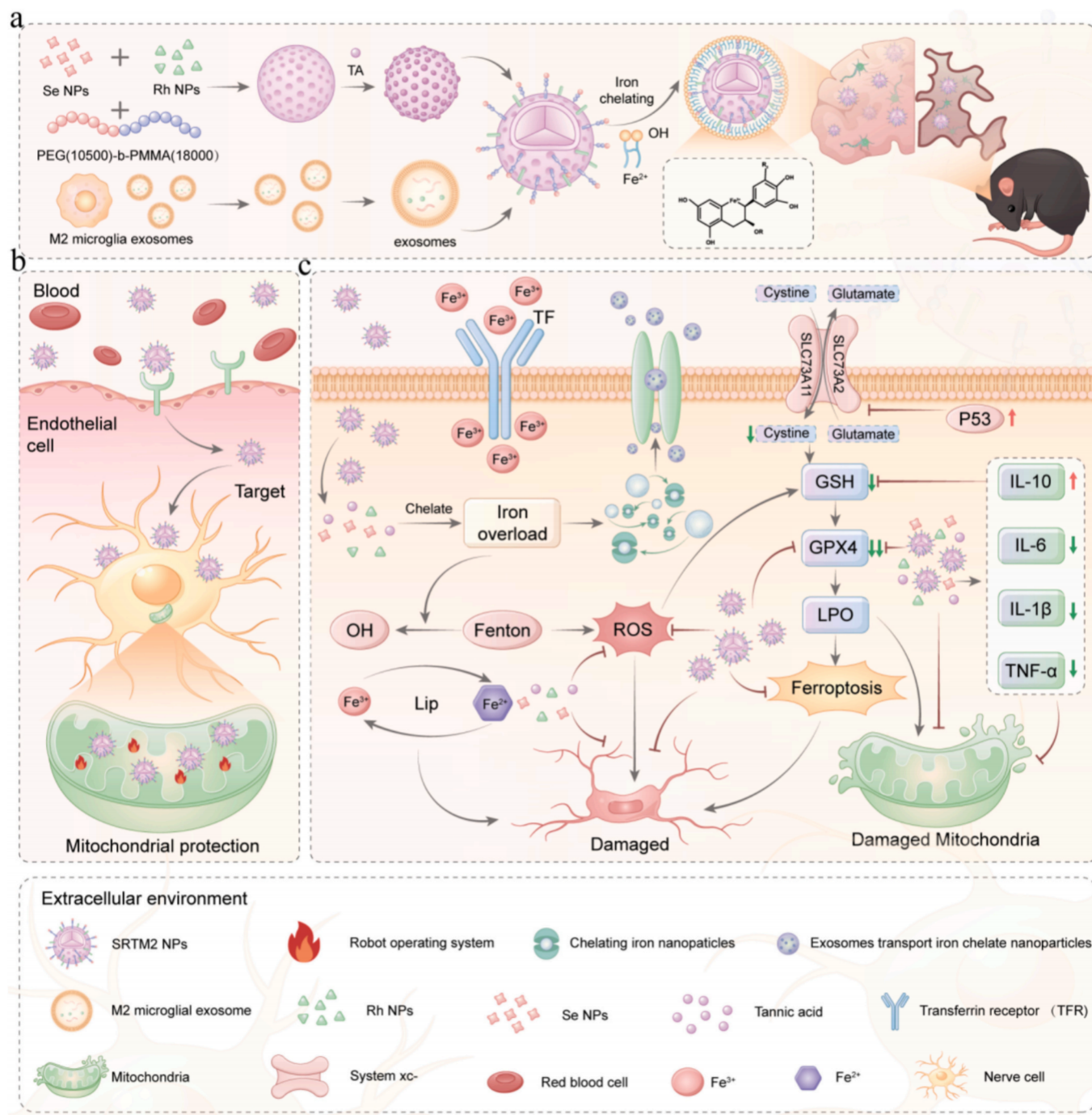
Fig. 1. The synthesis of SRTM2. a) Synthetic route of SRTM2. b-e) Transmission plots of Rh NPs, SR NPs, SRT NPs and SRTM2. f) SRTM2 element mapping diagram. g) Particle size of SRTM2 in different solutions. h) NTA analysis results of SRTM2. i) Western blot was used to detect the expression of characteristic proteins such as CD206, ALIX, and TSG101 in M2-type BV2 cells (with M0-type BV2 cells as the control) and M2-Exos cells (with M2-type BV2 cells as the control).

3. Results and discussion

3.1. Preparation and characterization of SRTM2 nanoparticles

The preparation of SRTM2 NPs involved several steps. The Se-mRh (SR) nanoparticles were successfully synthesized by chemical reduction method based on PEG (10500)-b-PMMA (18000), followed by further modification of Se-mRh nanoparticles by TA (SRT), encapsulation of microglia extracellular vesicles to the nanoparticles, and then,

SRT-encapsulated nanoparticles were washed and centrifuged to finally form SRTM2. The formation process and mechanism diagram of SRTM2 NPs are shown in Fig. 1a and Scheme 1. The prepared mRh NPs had a mesoporous loading morphology, uniform size, and high dispersion, which were characterized by transmission electron microscopy (TEM) (Fig. 1b). Subsequently, Se was doped into mRh NPs by a one-step reduction method (Fig. 1c). Furthermore, TA was further modified into Se-mRh NPs. Transmission electron microscopy (TEM) imaging revealed that the nanoparticles retained their mesopore while



Scheme 1. a) Visualization of the preparation process of SRTM2 and its role in chelating iron ions to alleviate brain lesions in Alzheimer's disease. b) A schematic representation illustrating the ability of SRTM2 to traverse the blood-brain barrier into neuronal tissue, as well as its localization within mitochondria. c) The targeting of ferroptosis by SRTM2 alleviates AD through three primary mechanisms: 1) Chelation of iron ions to reduce intracellular iron overload; 2) Regulation of the GPX4 signaling pathway to restore redox balance; 3) Modulation of mitochondrial function, clearance of reactive oxygen species (ROS), reduction in iron accumulation, and achievement of neuroprotection.

exhibiting higher density (Fig. 1d). It could be observed by scanning electron microscopy that the SRT nanoparticles had good dispersion and uniform size (Fig. S1). Finally, the SRT nanoparticles were encapsulated into the extracellular vesicles of M2-type microglia (Fig. 1e). Dynamic light scattering (DLS) analysis indicated that the average hydrodynamic

particle size of SRTM2 NP was between 80 nm and 120 nm (Fig. 1h). Furthermore, SRTM2 NP can be well dispersed in various types of solutions, and there is no significant change in particle size after 7 days of storage, indicating that SRTM2 has good stability (Fig. 1g). When SRTM2 is stored at -20°C for 4 weeks, it remains stable in terms of

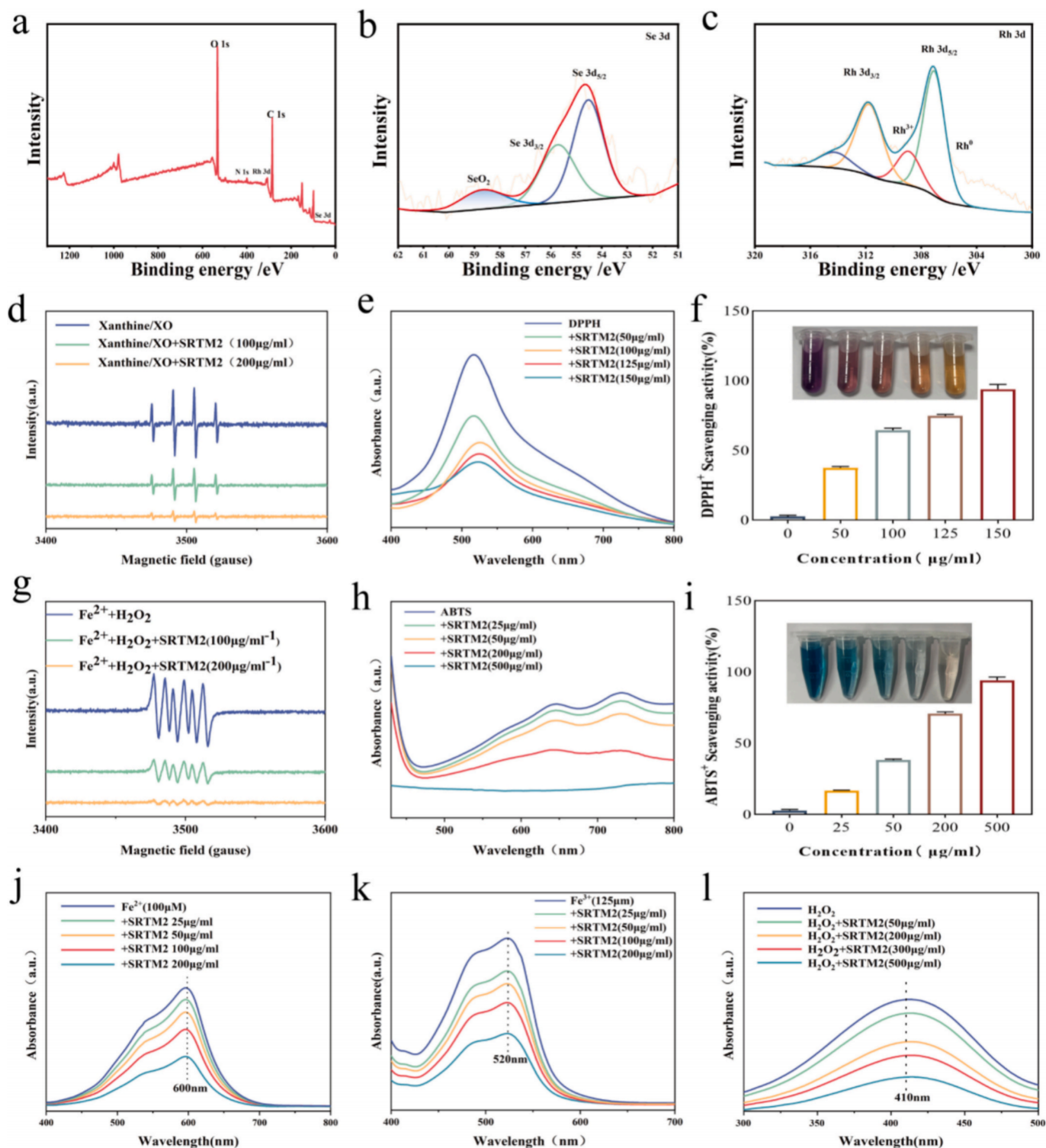


Fig. 2. a) XPS of Se-mRh. b) High-resolution XPS spectra of Se. c) Spectra of high-resolution xps mRh. The ESR spectra of the DMPO/•OH complex (g) and DMPO/O₂•-, (d) indicate the depletion of •OH and O₂•- after incubation with SRTM2 NPs. The antioxidant capacity of SRTM2 was determined by ABTS (h, i) and DPPH (e, f) methods. 1) The ultraviolet-visible absorption spectrum of hydrogen peroxide - titanium after the addition of SRTM2 indicates the H₂O₂ loss of SRTM2 (titanium sulfate method). j) Ultraviolet-visible absorption spectra of the blue tripyridine-triazine-Fe²⁺ complex after adding SRTM2 NPs. K) After the addition of SRTM2 NPs, the ultraviolet-visible absorption spectrum of the pink 2,2'-bipyridine-Fe³⁺ complex indicates the Fe³⁺ chelating ability of SRTM2 NPs.

morphology and particle size, and no significant differences are observed (Fig. S2). The elemental atlas (Fig. 1f) image further confirms the existence of Se and Rh elements. The ζ potential of M2-SeV is approximately -21.60 mV (Fig. S3), which is due to the presence of unbound carboxyl groups on the adhesion protein, and SRTM2 shows a more negative ζ potential. Western blotting and immunofluorescence analyses in Fig. S4 provided further evidence for the expression of M2-SeV markers, including CD9, ALIX, and TSG101 (Fig. 1i). As can be seen from Fig. 2a, the presence of Rh, Se, C, N and O elements was confirmed in the SRTM2 NPs XPS. Fig. 2c displays two prominent peaks at 312.05 eV (Rh (0) $3d_{5/2}$) and 307.26 eV (Rh (0) $3d_{5/2}$), accompanied by two minor peaks at 313.68 eV and 308.11 eV corresponding to Rh (III). Notably, Se-mRh NPs exhibit a slight positive shift in the Rh (0) $3d_{5/2}$ peak compared to mRh NPs, indicative of electronic structure modifications induced by Se doping. The Se 3d spectrum (Fig. 2b) reveals characteristic doublets at 55.02 eV (Se $3d_{3/2}$) and 54.11 eV (Se $3d_{5/2}$), with an additional oxidized Se peak observed at 58.69 eV.

Using DMPO as a spin probe, ESR spectroscopy revealed the ROS ($\cdot\text{OH}$ and $\text{O}_2\cdot^-$) scavenging capacity of SRTM2 nanoparticles (Fig. 2g). The DMPO/ $\cdot\text{OH}$ signal intensity decreased in a concentration-dependent manner upon SRTM2 NP treatment, confirming its $\cdot\text{OH}$ scavenging ability. Similarly, the DMPO/ $\text{O}_2\cdot^-$ signal was significantly attenuated by SRTM2 NP, with further reduction at higher concentrations (Fig. 2d), demonstrating strong $\text{O}_2\cdot^-$ clearance activity. Meanwhile, experiments

using 2, 2'-benzothiazolin-bis (3-ethylbenzothiazolin-6-sulfonic acid) (ABTS) (Fig. 2h, i) and 1, 1-diphenyl-2-oxylhydrazine (DPPH) (Fig. 2e, f) demonstrated that SRTM2 NP effectively cleared ABTS \cdot^+ and DPPH \cdot in a dose-dependent manner at 500 $\mu\text{g/mL}$. Their clearance rates reached 90% respectively. Then, the H_2O_2 removal capacity of SRTM2 NP was evaluated by the titanium sulfate method. Titanium sulfate can react with H_2O_2 to produce peroxide-titanium complexes by spectrophotometry, which can be inhibited in the presence of antioxidants. Considering the central role of iron in ferroptosis, iron chelation can more or less alleviate the cell death of iron-dependent ferroptosis in Alzheimer's disease. Therefore, we detected the chelating ability of Fe^{2+} and Fe^{3+} ions in SRTM2 NP. Fe^{2+} reacts with tripyridinyl triazine to form the blue tripyridinyl triazine- Fe^{2+} compound. Therefore, the chelating ability of Fe^{2+} ions in SRTM2 NP was evaluated by determining the level of tripyridinyl triazine- Fe^{2+} (Fig. 2j). As shown in Fig. 2j, in the presence of SRTM2 NP, the characteristic peak of tripyridinyl triazine- Fe^{2+} at 600 nm shows a concentration-dependent decrease, proving that SRTM2 has the activity of chelating Fe^{2+} . When Fe^{3+} coordinates with 2, 2'-bipyridine, it generates a distinctive pink complex monitored at 520 nm. The progressive signal diminution upon SRTM2 NP addition (Fig. 2k) directly evidences iron chelation activity. Similarly, the declining absorbance of peroxide-titanium complexes at 410 nm (Fig. 2l) quantitatively demonstrates H_2O_2 scavenging. This dual-action mechanism-simultaneously addressing oxidative stress and

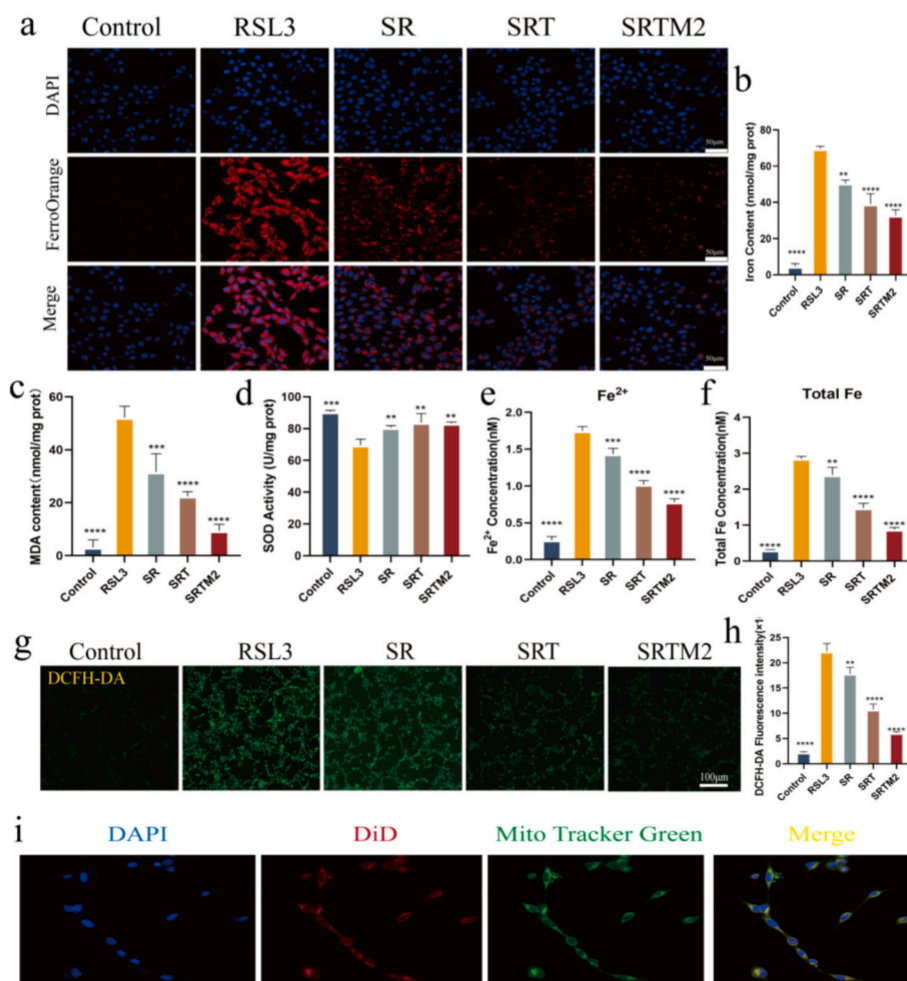


Fig. 3. SRTM2 maintains iron homeostasis by chelating free iron in mitochondria and removing reactive oxygen species. a) In RSL3-induced cells, SRTM2 chelates free iron in cytoplasm and mitochondria. b) Quantitative analysis of iron ions in SRTM2 chelate cells. c, d) Malondialdehyde (MDA) and superoxide dismutase (SOD) were quantified in HT22 cells induced by RSL3 for 12 h and/or treated with SRTM2 NPs for 24 h. e, f) Determination of iron content in HT22 cells induced by RSL3 for 12 h and/or treated with SRTM2 for 24 h. g, h) DCFH-DA analysis of ROS levels in cells of each group. i) Immunofluorescence analysis of MitoTracker and SRTM2 NPs of HT22 cells; Blue: DAPI, red: SRTM2 NPs, green: mitochondria. * $P < 0.05$, ** $P < 0.01$, *** $P < 0.001$, and **** $P < 0.0001$.

labile iron pools- establishes SRTM2 as a neuroprotective nanoplatform against AD-associated ferroptosis and oxidative damage.

3.2. *In vitro* study of SRTM2 NP targeting mitochondrial chelating Fe^{2+} to alleviate cellular ferroptosis

CCK-8 and cytotoxicity experiments indicated that the safe concentration of SRTM2 NP was $0\text{--}160\ \mu\text{g}/\text{mL}^{-1}$ within 12–24 h, which was the same for both BV2 and HT22 cells (Fig. S5). We induced ferroptosis in HT22 cells using GSH peroxidase 4 inhibitor (RSL3). We confirmed through live/dead cell staining (Fig. S6) that compared with the RSL3 group, the RSL3 + SRTM2 group effectively and significantly inhibited cell death. Furthermore, the detection results using the fluorescent probe Ferro Orange showed that RSL3 stimulation significantly increased the intracellular iron level of HT22 cells, proving the successful establishment of the iron-overloaded neuron model. Moreover, after SRTM2 treatment, this abnormally elevated iron level could be significantly reduced (Fig. 3a, b). Subsequently, the production of malondialdehyde (MDA) induced by RSL3 was detected. It can be found that the RSL3 + SRTM2 group can significantly inhibit the production of MDA (Fig. 3c). Detection of superoxide dismutase (SOD) in cells reveals that SRTM2 simultaneously has the effect of resisting the reduction of SOD induced by RSL3 (Fig. 3d). Based on this, we employed erastin to induce ferroptosis in cells, followed by the use of the C11-BODIPY fluorescent probe to detect intracellular lipid peroxidation (Fig. S10) and ROS levels (Fig. S11) after SRTM2 treatment. Furthermore, we observed that the erastin + SRTM2 group significantly inhibited MDA production and counteracted the erastin-induced decrease in SOD activity. (Fig. S12). Evaluation of cellular glutathione revealed that while RSL3 triggered GSH depletion in HT22 neuronal cells, SRTM2 treatment counteracted this effect by maintaining intracellular GSH stores (Fig. S6B). SRTM2 can chelate Fe^{2+} , thereby inhibiting the upregulation of Fe^{2+} and total iron content induced by RSL3 (Fig. 3e, f). We used DCFH-DA as the fluorescence probe to determine the intracellular ROS level. The detection results through inverted microscopy and flow cytometry showed that when HT22 cells were exposed to RSL3, the intracellular ROS level increased significantly [36]. However, when SRTM2 and RSL3 were co-incubated in the cells, the intracellular ROS level was significantly decreased (Fig. 3g, h). Furthermore, we labeled mitochondria with red fluorescent Mitotracker and SRTM2 with DiD to track the distribution of SRTM2 in HT22 cells (Fig. 3i). The results showed that SRTM2 could effectively target mitochondria. The above evidence indicates that SRTM2 can specifically target mitochondria, accumulate within the mitochondria of neurons, and chelate Fe^{2+} within neurons and eliminate a large amount of ROS within neurons.

3.3. *SRTM2 exerts neuroprotective effects by reducing iron-dependent mitochondrial oxidative damage*

Due to the fact that excessive intracellular iron ions tend to transfer into mitochondria and activate the Fenton reaction, leading to the outbreak of cellular oxidative stress [37], in the above experiments, we have concluded that SRTM2 has the ability to target mitochondria and chelate intracellular Fe^{2+} , which can effectively reduce the retention of intracellular iron ions. The analysis was shown using immunofluorescence imaging. A large amount of $\text{A}\beta$ can reduce the content of kernel factor-associated factor 2 (Nrf2).

Compared with SRT treatment, SRTM2 treatment can more significantly inhibit the decrease in intracellular Nrf2 level induced by $\text{A}\beta$ (Fig. 4a, b). Furthermore, Mito-SOX staining for mitochondrial ROS specific recognition also indicated that SRTM2 treatment exhibited the most prominent performance in inhibiting the generation of ROS within mitochondria (Fig. 4c, d). These results strongly support the view that SRTM2 targeting mitochondria can maximize the resistance to oxidative stress caused by iron deposition. Extensive research has demonstrated that oxidative stress triggers both depolarization of mitochondrial

membrane potential and membrane rupture through phospholipid oxidation. JC-1 staining revealed that the red fluorescent JC-1 aggregate was inhibited after stimulation by $\text{A}\beta$ [38], but significantly recovered after SRTM2 treatment, and at the same time prevented the production of $\text{A}\beta$ -induced JC-1 with green fluorescence (Fig. 4e, f). SRTM2 treatment is more effective than SR and SRT treatments in rescuing the decline of mitochondrial membrane potential induced by $\text{A}\beta$. As indicated by the higher proportions of aggregates and monomers, the SRTM2 treatment group is closer to the control group. Furthermore, we also detected ferroptosis in HT22 cells through Western blotting. As expected, under RSL3 stimulation, the expression of the Nrf2 gene was significantly downregulated (Fig. 4h, g), and the protein levels of its downstream components GPX4 and SLC7A11 were substantially decreased. Treatment with SR, SRT, and SRTM2 increased their expression, but the effect of the latter was more pronounced than that of the former (Fig. 4i, j). Experimental data demonstrated that SRTM2 treatment effectively counteracted the RSL3-induced ferroptotic effects, significantly reducing the expression of pro-apoptotic markers (Bax and caspase-3) (Fig. 4l–n) while restoring the levels of the anti-apoptotic protein Bcl-2 (Fig. 4k, m). In conclusion, SRTM2 enhances the Nrf2-mediated elimination and antioxidant network of paper peroxidation, thereby strengthening the defense system against $\text{A}\beta$ -induced neuronal damage.

3.4. *SRTM2 inhibit neuronal apoptosis and secretion of pro-inflammatory cytokines in vitro*

Studies have shown that organic nanoparticles exhibit unique intracellular transport and extracellular secretion behaviors in microglia, while inorganic nanoparticles inhibit the transmission of the ERK1/2 signaling pathway and the release of EVs, resulting in the long-term retention of NP in microglia and preventing NP from being cleared from the brain [34]. Therefore, the deposition of NP in the brain can be effectively cleared by increasing the extracellular vesicles released by microglia. To determine the absorption capacity of target cells for SRT and SRTM2 and their intracellular deposition time, we labeled SRT and SRTM2 nanomedicines with fluorescein isothiocyanate and DiD dye respectively, and then incubated them with microglia for different periods of time. The findings indicated that HT22 cells effectively internalized both SRT and SRTM2 in a time-dependent fashion (Fig. 5a–b), indicating that they could be absorbed by target cells. Subsequently, we investigated the promotion of nanoparticle excretion by SRTM2 after its reuptake by cells. We observed the intracellular residence time of SRTM2 using a laser confocal microscope. The results showed that the uptake peaked at 12 h, while the intracellular fluorescence signal of SRTM2 decreased significantly at 24 h. Conversely, we observed the intracellular residence time of SRT. It can be observed that the fluorescence signal of SRT at 24 h is significantly increased compared with that at 12 h. This indicates that SRTM2 can not only be rapidly absorbed by cells, but also subsequently rapidly promote the excretion of nanoparticles within cells and prevent the deposition of nanomedicines within cells (Fig. 5d, e). Following this, we studied SRTM2's capacity to traverse the blood-brain barrier and its apoptosis-inhibiting properties. An *in vitro* BBB model was used for permeability evaluation (Fig. 5c). Before the incubation of nanomedicines, the successful establishment of the model was demonstrated by the endothelial resistance (TEER) value exceeding 200Ucm^2 . The TEER value remained stable after incubation, indicating that SRTM2 did not damage the integrity of bEnd3 cells (Fig. S7). The neuroprotective effect of SRTM2 was evaluated through neuronal apoptosis analysis. Biological projection electron microscopy showed that after $\text{A}\beta$ induction, the mitochondrial membrane density increased, the cristae decreased or even disappeared. After SRTM2 treatment, both the mitochondrial membrane density and the cristae were significantly restored, and the recovery effect was obvious due to SRT treatment (Fig. 5g). Flow cytometric analysis with Annexin V-FITC/PI staining was then employed to assess $\text{A}\beta$ -induced neuronal apoptosis.

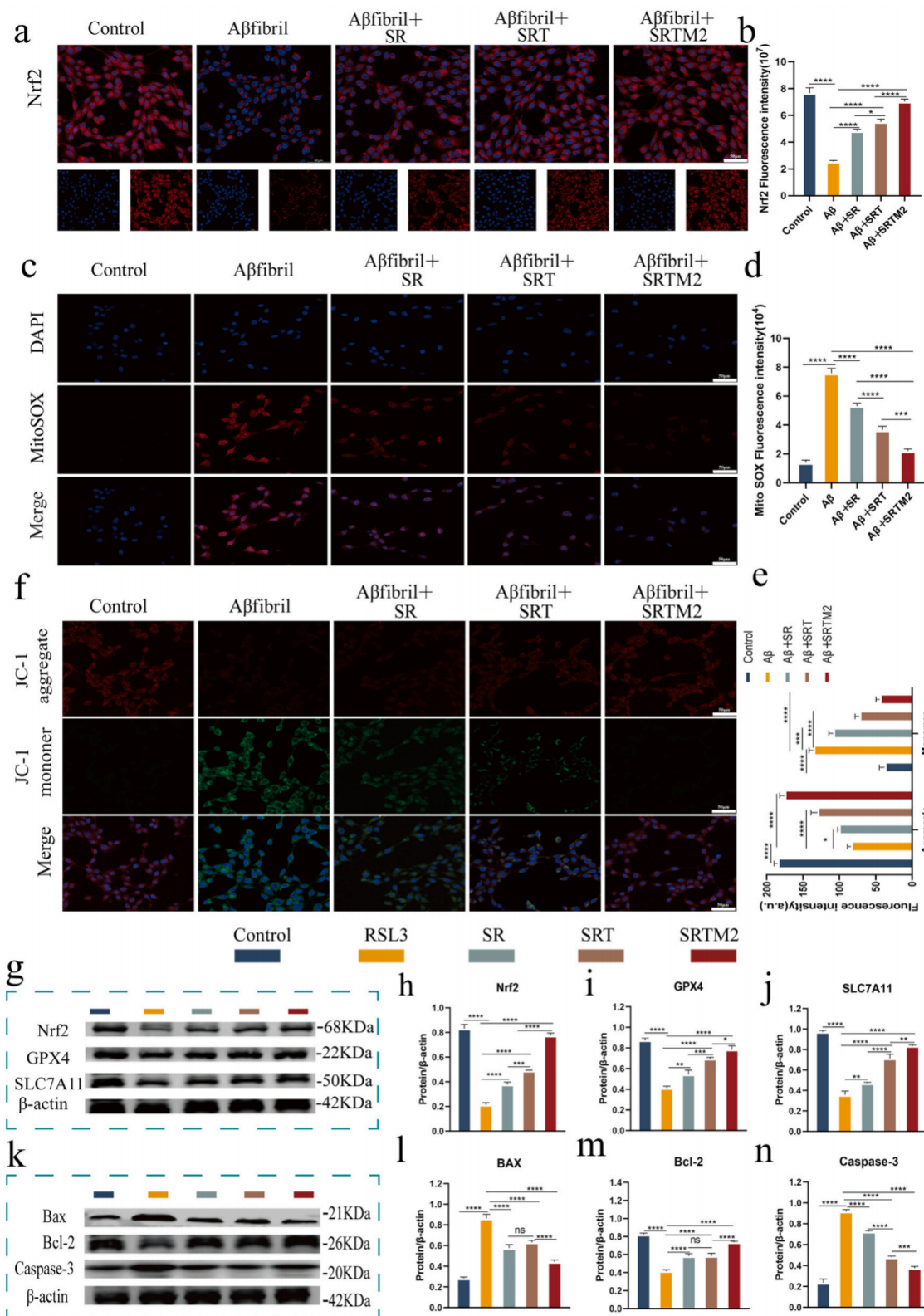


Fig. 4. SRTM2 demonstrates neuroprotective effects by mitigating Aβ-induced oxidative stress and mitochondrial dysfunction. a, b) Representative immunostaining images of Nrf2 protein in HT22 cells, accompanied by quantitative analysis of fluorescence intensity. c, d) Representative confocal fluorescence images along with quantitative analysis of Mito-SOX staining. Scale bar: 50 μm. e, f) Representative confocal fluorescence images and corresponding quantitative analysis of JC-1 staining. Red indicates JC-1 aggregates; Green represents JC-1 monomers. Scale bar: 50 μm. g-j) Representative western blotting results and quantitative analysis for Nrf2, GPX4, and SLC7A11. k-n) Representative western blotting results and quantitative analysis for Bax, Bcl-2, and Caspase-3. *P < 0.05, **P < 0.01, ***P < 0.001, and ****P < 0.0001.

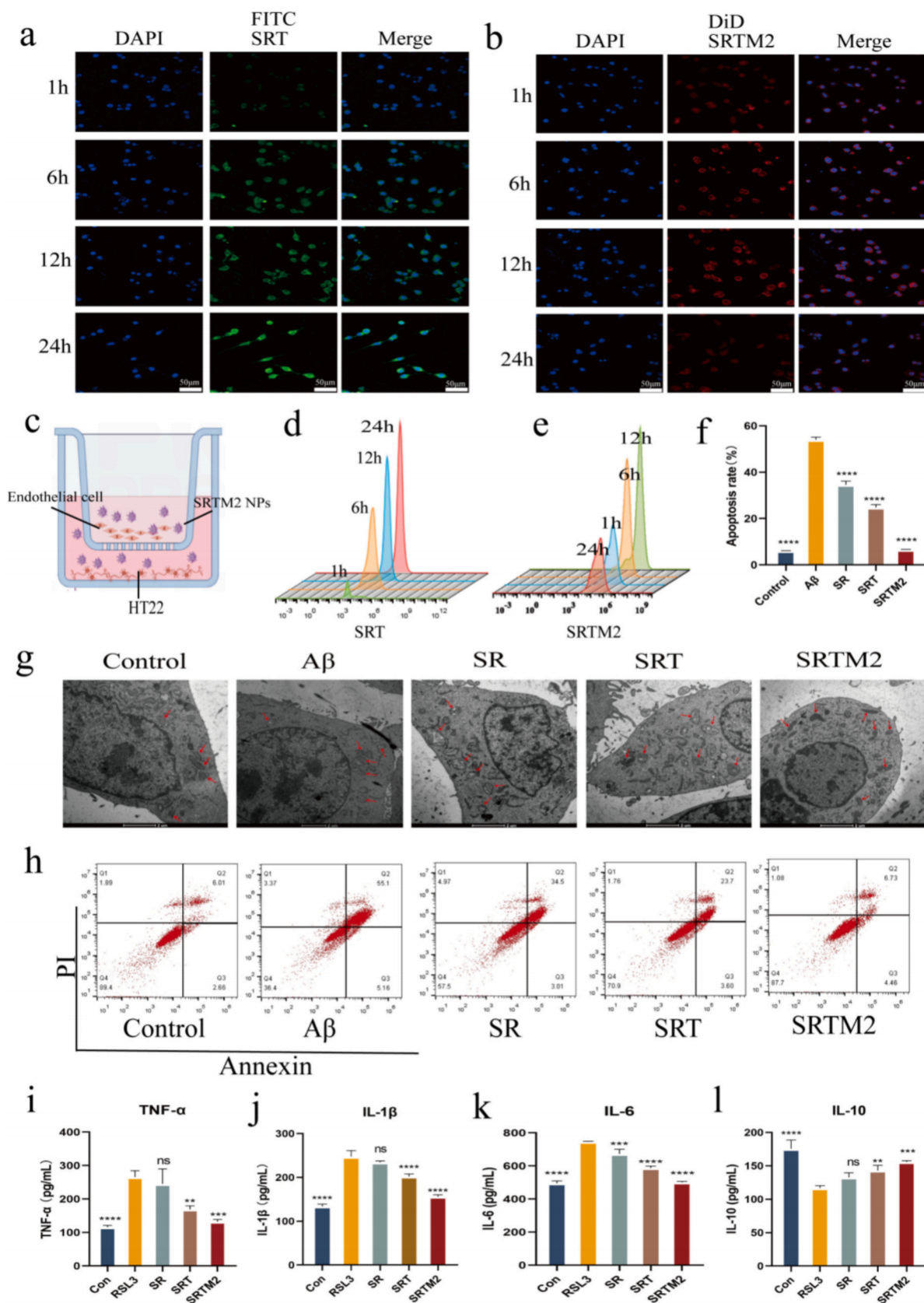


Fig. 5. Confocal laser scanning microscopy images of (a, b) FITC-SRT NPs and DiD-SRTM2 at different time points (scale: 50 μm). c) SRTM2 crossed the blood-brain barrier model in vitro. d, e) Quantitative map of cell uptake of SRT and SRTM2. g) Representative transmission electron microscope images of mitochondrial morphology in HT22 cells after different treatments. The red arrows represent mitochondria (Scale: 500 nm). h) Quantitative statistics of neuronal apoptosis and (f) apoptosis rate after different treatments were analyzed by flow cytometry. i-l) elisa analysis of cellular inflammatory factors TNF-α, IL-6, IL-10 and IL-1β. * $P < 0.05$, ** $P < 0.01$, *** $P < 0.001$, and **** $P < 0.0001$.

The results showed that SRTM2 treatment reduced the apoptosis rate of HT22 cells from 55.1% induced by A β to 6.73%, which was more effective than 23.7% of SRT treatment (Fig. 5f, h). These findings emphasize that SRTM2 has the ability to inhibit A β -induced neuronal apoptosis and maintain neuronal viability. The study also assessed how SRTM2 affected HT22 cell activation and cytokine release. A β -induced neurons showed elevated TNF- α , IL-1 β , and IL-6 expression, but these pro-inflammatory markers were significantly downregulated by SRTM2 (Fig. 5i-k). In addition, SRTM2 enhances the production of anti-inflammatory cytokine 10 (IL-10) in A β -induced neuronal cells (Fig. 5l). To assess the activation status of upstream inflammatory pathways, we performed Western blot analysis of key signaling molecules. The results showed that, compared with the model group, SRTM2 treatment significantly increased the protein levels of p-PI3K, p-AKT, and p-mTOR (Fig. S13), indicating activation of the crucial PI3K/AKT/mTOR signaling axis involved in cell survival and anti-inflammatory responses. Furthermore, it suppressed the expression of NF- κ B. Activation of this pathway can directly inhibit the transduction of pro-inflammatory signals. The immunofluorescence results showed that the level of Bax in RSL3 stimulation increased (Fig. S9), and the expression level of GPX4 decreased (Fig. S8). The SR and SRT groups could slightly improve the expression of the two proteins, but the SRTM2 group improved these results more significantly. Given its ability to counteract oxidative stress, diminish neuronal apoptosis, and block pro-inflammatory cytokine production, SRTM2 shows promising therapeutic effects in managing inflammation and improving cell survival within AD lesion areas.

3.5. Therapeutic mechanism of SRTM2 on AD through transcriptome analysis of cells

To better understand the involvement of SRTM2 in initiating the endogenous antiferritin imbalance pathway for AD intervention, we conducted transcriptomic analyses on HT22 cells treated with A β and HT22 cells co-incubated with A β and SRTM2. The Venn diagram as shown in the figure (Fig. S14) indicates that a total of 11,390 genes were expressed in the two groups of samples, while only 342 genes were expressed in the A β + SRTM2 group. Volcano maps showed that in the A β + SRTM2 group, 822 differentially expressed genes were upregulated and 293 differentially expressed genes were downregulated (Fig. 6a). Potential pathways contributing to AD progression were revealed through KEGG pathway analysis (Fig. 6b), and central genes related to ferroptosis were also discovered. That is, GPX4, ferritin heavy chain (FTH1), Member 11 of the solute carrier family 7 (SLC7A11), etc. Among them, GPX4 is the hub gene causing ferroptosis (Fig. 6c). Functional analysis indicated.

that the differentially expressed genes in the SRTM2 treatment group were mainly involved in neurological development, synaptic systems, behavior, memory and learning cognition, such as neuronal generation, neurological development, neuronal projection and synapses. These differentially expressed genes were significantly regulated (Fig. 6d). Further gene expression analysis revealed that compared with the A β group, the expression of apoptotic genes such as Bcl2, Pik3cd, and Birc5 was upregulated in the SRTM2 treatment group, while the expression of genes such as Bax, Tnfrsf1a, and Map2k1 was downregulated (Fig. 6e). The expressions of ferroptosis-related genes SLC7A11 and GPX4 were upregulated, while the expressions of ferroptosis-promoting genes such as Cs, Emc2, Vdac2, and Lpcat3 were downregulated (Fig. 6f). Further analysis of the indications of inflammation-related genes showed that related genes such as Tapbp and Hif1a were upregulated. Down-regulation of related genes such as Gna13, Tnfrsf1b, and Cdkn1a (Fig. 6g). These findings indicate that ferroptosis is strongly associated with the onset and progression of AD, suggesting that targeting this process could be a potential therapeutic strategy.

3.6. Evaluate the cognitive improvement of AD mice treated with SRTM2 through behavioral assessment

Next, we will explore the therapeutic effect of SRTM2 in alleviating cognitive impairment in a mouse model of AD. As shown in the experimental protocol (Fig. 7a), SRTM2 will be injected into the tail vein of 9-month-old AD mice every three days for seven consecutive times. After three weeks, the cognitive behaviors of each group of mice will be evaluated through water maze, Y-maze and open mill experiments. Firstly, we conducted a water maze experiment on mice to test their spatial learning and memory abilities. During the navigation and orientation stage of the hidden platform [39], the escape latency of AD mice significantly increased, while after SRTM2 treatment, the escape latency of AD mice was significantly shortened, almost approaching that of WT mice (Fig. 7e), indicating a significant improvement in learning disabilities. Finally, on the 6th day, we conducted tests on the mice. First, we carried out the spatial exploration stage of removing the platform (Fig. 7b). AD mice showed a more severe stereotyped behavior of boundary search [40], while mice treated with SRTM2 searched in the area where the original platform was located. Similar to WT mice, the distance and time in the target quadrant increased significantly (Fig. 7f, g). Meanwhile, the swimming speed of the mice also increased slightly (Fig. 7h) and the number of times they crossed the platform also increased (Fig. S15). For the Y-maze experiment, we need to open the arms that were closed during the training phase during the testing phase to check whether the mice will be attracted to the new arms. It can be seen that WT mice prefer to stay on the new arms to perform repetitive movements and explorations, while AD mice show the opposite behavior [41], which can be seen from the fact that AD mice have fewer trajectories in the new arms (Fig. 7c). After SRTM2 drug treatment, AD mice regained a stronger desire to explore new arms compared to before, almost the same as WT mice, and there were significant increases in both the time and distance percentages of new arms (Fig. 7i, j). Based on this, we conducted a novel object recognition test in mice to evaluate improvements in non-spatial memory. The results showed that mice treated with SRTM2 exhibited significantly prolonged exploration time toward the novel object, as illustrated in Fig. S17. Finally, we conducted the open field test (OFT) on the mice to further evaluate their autonomous exploration ability (Fig. 7d). Compared with AD mice, the time and distance of peripheral activities in the SR, SRT, and SRTM2 groups were all improved (Fig. S16). It can be intuitively observed from the movement trajectory that AD mice spent more time and distance in the periphery and less time and distance in the central area. However, mice treated with SRTM2 drug resumed the behavior of exploring the internal space, similar to WT mice (Fig. 7k, l), indicating that the exploration motivation in the new environment has been significantly improved. In conclusion, these results can prove that SRTM2 treatment can reverse the decline of spatial memory ability in AD model mice.

3.7. Brain targeting and safety evaluation of SRTM2 in vivo

Before conducting in vivo experiments, we had carried out hemolysis experiments to detect the biosafety of SRTM2. The results showed that within 4 h of co-incubation, the erythrocyte membrane was not damaged, and the hemolysis rate of all samples was less than 5% (Fig. S19), indicating that the nanoparticles have good blood compatibility. Based on this, we administered different doses of the drug to mice via tail vein injection to evaluate its efficacy and safety. In the high-dose group, some blood biochemical parameters (such as liver and kidney function-related indicators) showed abnormal fluctuations (Fig. S18). This suggests that a dose of 4.5 mg/kg may alter the internal microenvironment of the mice, potentially impairing their liver and kidney function. No such abnormalities were observed in the 1.5 mg/kg or 3 mg/kg groups. To evaluate the accumulation and biodistribution of SRTM2 in the brain, DiD-labeled SRTM2 was injected into the tail vein of mice. Subsequently, the distribution of SRTM2 in the body was observed

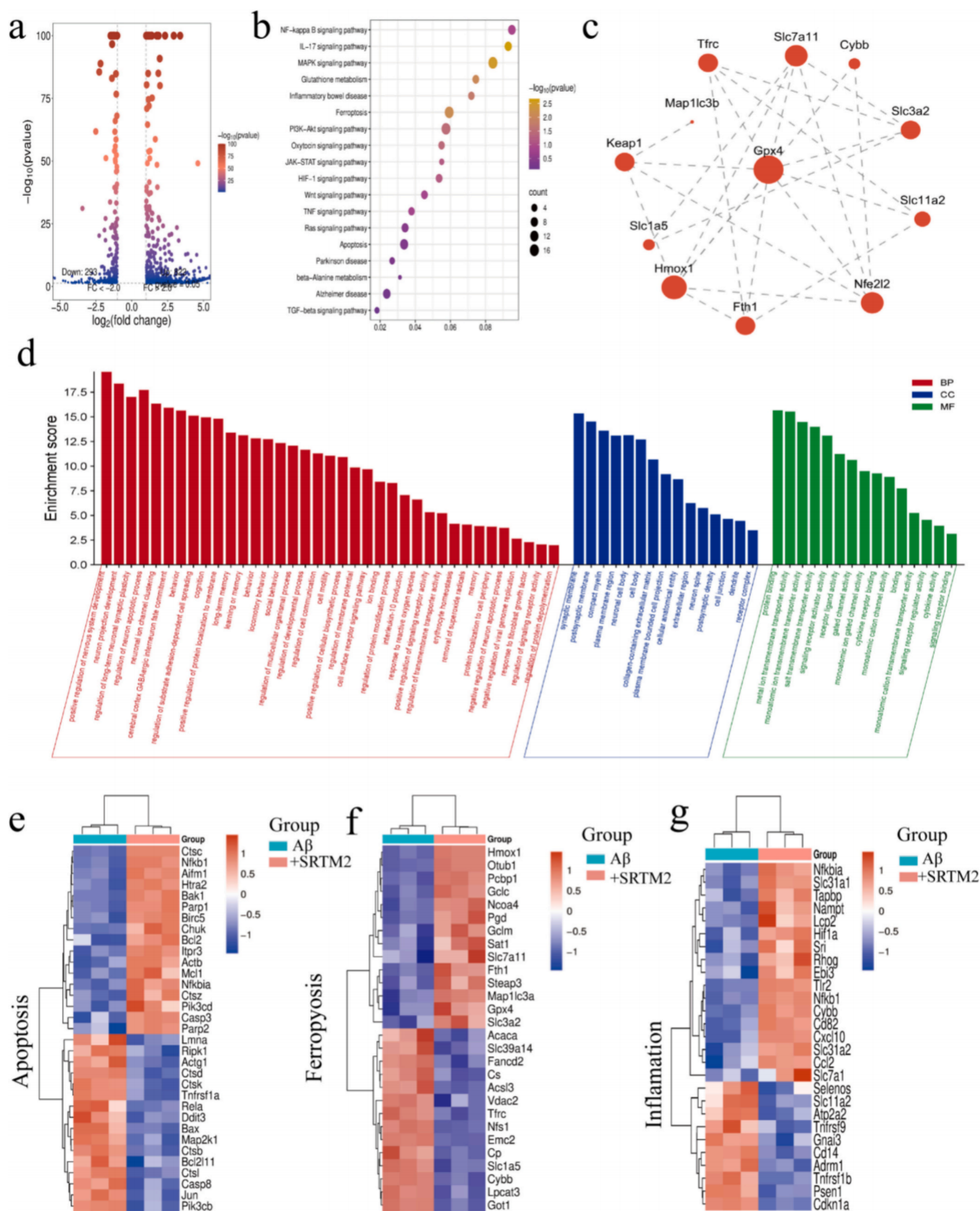


Fig. 6. a) Volcano map showed the DEGs between Aβ treatment group and SRTM2 treatment group, with 293 down-regulated genes and 822 up-regulated genes highlighted. b, c) KEGG pathway enrichment analysis and differentially expressed genes (DEGs) enrichment of iron-death related genes in Aβ treatment group and SRTM2 treatment group. d) DEGs enrichment analysis of related pathways between Aβ treatment group and SRTM2 treatment group (BP: biological process; CC: cell component; MF: Molecular function). e-g) DEGs associated with iron death, apoptosis, and inflammation in the SRTM2 and Aβ groups. SE is expressed as mean ±. Univariate analysis of variance and Tukey post hoc test were used for statistical significance analysis.

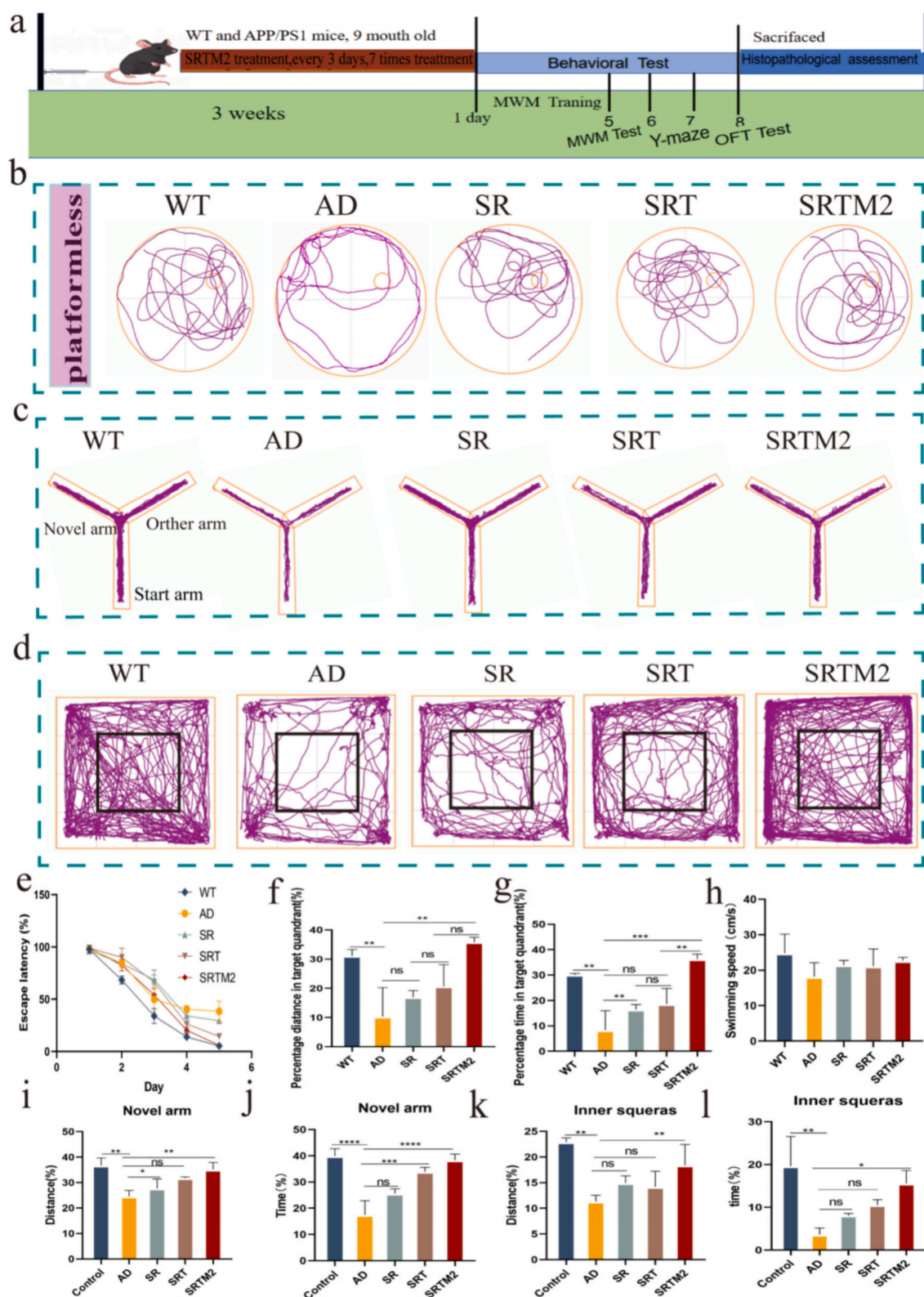


Fig. 7. SRTM2 therapy improves cognitive impairment in AD mice. **a)** Animal experiment schedule: WT mice were treated with PBS, AD mice were treated with SR, SRT and SRTM2, and injected into the tail vein once every 3 days, a total of 7 times. MWM, Y and open field tests were performed on mice to assess memory and learning ability. **b)** Swimming path map of mouse MWM experiment. **c)** Mouse Y maze experiment path map. **d)** Mouse open field experiment path map. **e)** Mice escape latency during training. **f, g)** Time and distance of the mice in the target quadrant. **h)** Swimming speed of mice. **i, j)** The time and distance of mice in the new arm in the Y maze experiment. **k, l)** Time and distance of mice in the central region in open field experiments. Data are expressed as mean \pm SEM ($n = 8$). * $P < 0.05$, ** $P < 0.01$, *** $P < 0.001$, and **** $P < 0.0001$.

using an *in vivo* imaging system. Images of mice were taken at different times. The results showed that the distribution of DiD-labeled SRTM2 in the brain gradually increased over time. The peak can be observed at the 6th hour. Subsequently, the fluorescence signal of SRTM2 gradually weakens and disappears. During the same period, at least a small amount of SR and SRT drugs pass through the blood-brain barrier. However, when the metabolism of SRTM2 is about to be completed, SR and SRT show high-intensity fluorescence signals. It indicates that SRTM2 has the function of rapidly crossing the blood-brain barrier and quickly clearing nanoparticles after the nanomedicine takes effect in the body, preventing the deposition of nanomedicine in the body and causing inflammation again (Fig. 8a, b). Then, *in vivo* fluorescence imaging of the major organs was performed. Observation revealed that the fluorescence intensity differences in brain tissues were somewhat inconsistent with the *in vivo* imaging results (Fig. 8c-e). At 48 h post-administration, minimal amounts of SR and SRT, along with a small quantity of SRTM2, were found to accumulate in the liver. This reflects the normal metabolic pathway of nanoparticles through the liver. As the primary organ of the reticuloendothelial system, the liver serves as the central site for clearing exogenous nanoparticles and vesicles from the bloodstream, resulting in relatively slow intrahepatic metabolism and excretion. Therefore, the signal from the liver does not indicate abnormal accumulation. Meanwhile, to evaluate the biocompatibility of SRTM2 with living organs and tissues, histological analysis was conducted on the major organs (heart, liver, spleen, kidney) of C57 mice injected with the SRTM2 nanocomposite. Compared with the PBS group, no obvious pathological abnormalities were found in the tissues of mice injected with SRTM2 (Fig. 8f). The body weight of mice was detected for 21 consecutive days, and no significant increase or decrease was observed in the body weight of the mice (Fig. S20). Frozen sections were prepared using mouse brain tissue for the detection of fluorescence signals. Representative confocal microscope images of mouse brain sections showed that the hippocampus and cortex highly took up DiD labeled SRTM2, which was widely distributed throughout the brain (Fig. S21). Additional hematological and biochemical examinations of blood samples were carried out. Results indicated normal ranges for all tested parameters in the SRTM2 group, offering further confirmation of the compound's biosafety (Fig. S23). This indicates that SRTM2 can effectively penetrate the blood-brain barrier and is a natural carrier for the treatment of neurological diseases. This indicates that SRTM2 can rapidly pass through the blood-brain barrier and does not cause obvious abnormalities such as hepatotoxicity or nephrotoxicity during the treatment process.

3.8. SRTM2 inhibits ferroptosis and inflammation *in vivo*

Based on behavioral science, we euthanized the mice and collected their brain tissues to characterize the changes in the relevant pathological states in the brain [42]. The activation status of microglia in the mouse brain was observed by immunofluorescence staining. The microglia and astrocytes in the cortex and hippocampus of AD mice were significantly activated, manifested as an increase in the number of IBA1+ microglia and GFAP astrocytes. SRTM2 treatment inhibited the increase of microglia and astrocytes in the AD brain, indicating that SRTM2 has an anti-neuroinflammatory effect (Figs. S24–25). Subsequently, we used Prussian blue staining to further detect the distribution of iron deposits in the mouse brain. A large number of iron deposit plaques were observed in the hippocampus and cortex of AD mice [43]. After SRTM2 treatment, these plaques were significantly eliminated (Fig. S26). Furthermore, to exclude potential interference from the inherent iron-chelating activity of the SRTM2 component and to conduct a more accurate assessment, we performed quantitative verification using inductively coupled plasma mass spectrometry (ICP-MS) to detect the iron-chelating effect of SRTM2 (Fig. S27). The results indicated that SRTM2 treatment could effectively reduce iron deposits in the brain of AD lesions. The protein level of Caspase-3 in the brain of mice was

detected by immunofluorescence. It was observed that the content of Caspase-3 in the brain of AD mice increased significantly. After treatment with SRTM2, the content of Caspase-3 decreased significantly (Fig. 9a). The condition of neuronal injury in the mouse brain was further evaluated by immunofluorescence, as shown in Fig. 9b. Neuronal injury was significantly improved in the SR, SRT, and SRTM2 groups, while the number of neuronal injuries in the AD mouse brain increased and the fluorescence signal was weak. In addition, the deposition of A β was detected by immunofluorescence staining and Nissl staining, as shown in (Fig. 9c f). The hippocampal sections of AD mice showed a large number of A β plaques and a large number of fluorescent spots, which formed a sharp contrast with WT mice. Meanwhile, in the SR, SRT, and SRTM2 groups of mice, it could be observed that the fluorescence signals were significantly reduced. This indicates that the content of A β significantly decreased after administration. Notably, in the SRTM2 group, almost no fluorescent spots were detected, and the content of A β in the brain almost decreased to the same level as that of normal mice. In addition, we also detected the levels of oxidative stress and inflammatory factor Nrf2 in the brain tissue by immunofluorescence [44]. It was observed that the expression of Nrf2 in the brain tissue of AD mice was significantly decreased. After treatment with SRTM2, the content of Nrf2 in the brain tissue of mice increased significantly. This indicates that the nanomedicine SRTM2 plays a crucial role in inhibiting oxidative stress and reducing inflammation in AD mice (Fig. 9g). Overall, through the above experiments, it has been proved that SRTM2 nanoparticles can effectively reduce the burden of A β , alleviate oxidative stress, and prevent the death of brain neurons in AD mice. To further clarify the potential regulatory mechanism of SRTM2 treatment on various influencing factors affecting ferroptosis, the expressions of related proteins in Nrf2-mediated iron metabolism and endogenous antioxidant and anti-apoptotic pathways were determined by Western blotting. Along the upregulation of Nrf2 (Fig. 9d), the levels of downstream LPO detoxification enzymes GPX4 and SLC7A11 in the brains of AD mice treated with SRTM2 were significantly increased (Fig. 9e). Subsequently, the ROS levels in the brains of the mice were detected. As expected, the ROS levels of AD mice showed a red fluorescence signal, which was much higher than that of WT mice. After SRTM2 treatment, oxidative stress was significantly relieved, proving that SRTM2 can exert neuroprotective effects by preventing cell apoptosis and reducing oxidative stress in the brain (Fig. 9h, i). Subsequently, the levels of inflammatory cytokines in the mouse brain tissue were detected using ELISA kits (Fig. S22). In the SR, SRT and SRTM2 treatment groups, the expressions of pro-inflammatory factors (IL-1, IL-6, TNF- α) decreased to varying degrees. The expression of anti-inflammatory factor (IL-10) increases. Generally speaking, SRTM2 can simultaneously initiate multiple pathways to treat AD.

4. Conclusion

This study indicates that the dynamic regulation of intracellular unstable iron ponds (LIP) plays a key role in inhibiting ferroptosis and intervening in the process of AD [45]. LIP as the main storage form of free iron and REDOX active iron, its abnormal accumulation in mitochondria (mLIP) and lysosomes can catalyze the burst of reactive oxygen species (ROS) and the coupling reaction of lipid peroxidation through the Fenton reaction, thereby driving the occurrence of ferroptosis. This process is closely related to the neurodegenerative changes of AD [46]. Based on the above mechanism, this study designed a multifunctional composite nanomedicine SRTM2. Its core innovation lies in interfering with the ferroptosis signal network through the synergistic action of multiple targets, while taking into account the multi-dimensional regulation requirements of the AD microenvironment: On the one hand, by eliminating ROS, reducing the accumulation of Fe²⁺ in the cytoplasm and mitochondria, and up-regulating the expression of glutathione peroxidase 4 (GPX4), the intracellular antioxidant capacity is enhanced and iron metabolic homeostasis is maintained; On the other

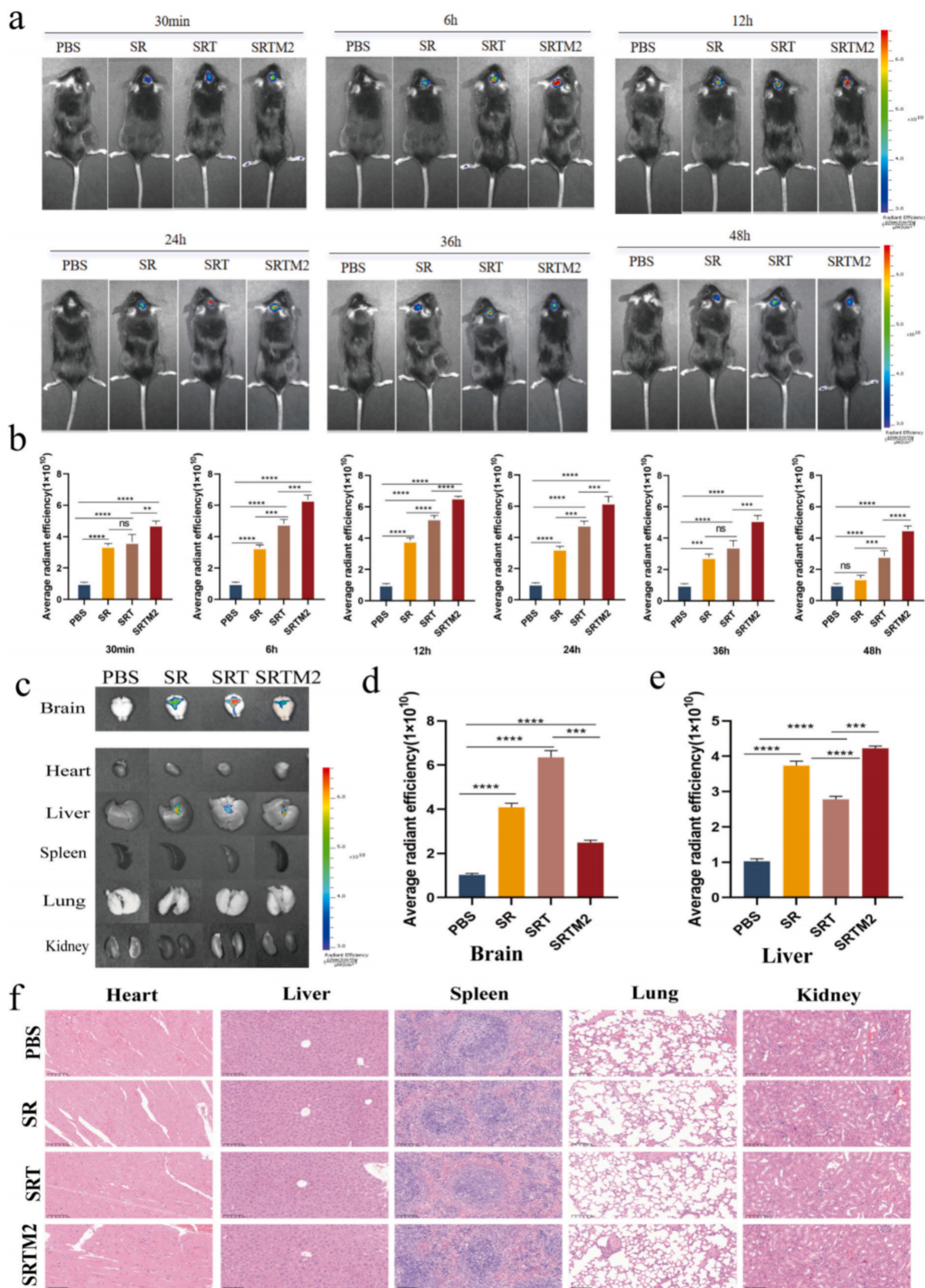


Fig. 8. To evaluate the brain targeting effect and biosafety of SRTM2. a, b) FITC-labeled SR and SRT, DiD-labeled SRTM2 (8 mg/kg) C57BL/6 J mice with representative fluorescence images in vivo and quantitative analysis of brain fluorescence intensity at different time points. c) In vitro fluorescence images of major representative organs 48 h after administration. d, e) Quantitative fluorescence analysis of brain and liver at 48 h after administration. f) Hematoxylin and eosin staining of major organs after injection of different nanoparticles (scale = 50 μ m). Data are expressed as mean \pm SEM ($n = 3$). * $P < 0.05$, ** $P < 0.01$, *** $P < 0.001$, and **** $P < 0.0001$.

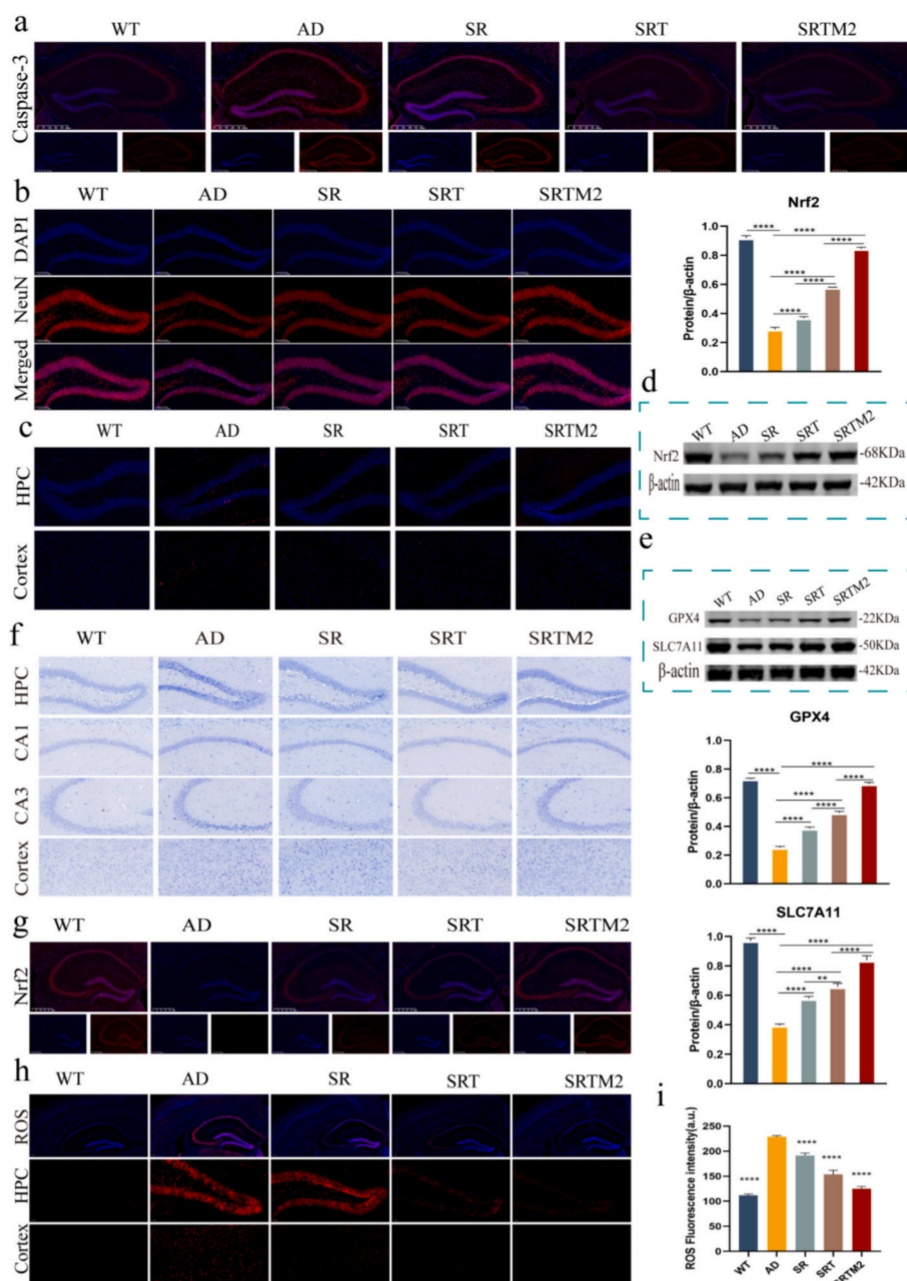


Fig. 9. a) Immunofluorescence plot of Caspase-3 protein expression in the mouse brain. b) Immunostaining of NeuN-positive cells in HPC of AD mice. c) Immunofluorescence plots of A β in the brains of different mice. d) Representative WB bands and statistical results of Nrf2 and e) Nrf2 signaling pathway-related proteins (GPX4 and SLC7A11). f) Nissl staining of different regions of the brain of AD mice. g) Expression of Nrf2 protein content in the brain of AD mice. h-i) The expression and statistical results of ROS in the hippocampus and cortical regions of AD mice. * $P < 0.05$, ** $P < 0.01$, *** $P < 0.001$, and **** $P < 0.0001$.

hand, by targeting mitochondrial function regulation, inhibiting the generation of mROS and blocking the release of Fe²⁺ from mLIP to the cytoplasm, the triggering of ferroptosis can be effectively contained. Compared with the traditional single-target therapeutic strategy, the multi-targeting feature of SRTM2 can intervene more precisely in the complex microenvironment imbalance of AD, including multi-cellular interaction networks such as neuroinflammation, oxidative stress and iron metabolism disorders. The experimental results show that SRTM2 exhibits significant advantages in inhibiting neuronal ferroptosis and improving the pathological characteristics of AD. Furthermore, this nano-delivery strategy centered on ferroptosis not only provides new ideas for the treatment of AD, but also opens up potential application prospects for the intervention of other neuroinflammation-related diseases. Future research will further optimize the targeted delivery

efficiency of SRTM2 and explore its potential in the clinical transformation of neurodegenerative diseases, with the aim of providing a scientific basis for the precise regulation of brain health homeostasis.

CRediT authorship contribution statement

Chaonan Jing: Methodology, Investigation, Data curation. **Kezhen Ge:** Formal analysis, Data curation, Conceptualization. **Dehong Yu:** Investigation, Data curation, Conceptualization. **Minghao Chao:** Formal analysis, Data curation, Conceptualization. **Yiming Yin:** Formal analysis, Data curation, Conceptualization. **Junjie Li:** Formal analysis, Data curation, Conceptualization. **Yufan Liu:** Formal analysis, Data curation, Conceptualization. **Guangyu Ma:** Formal analysis, Data curation, Conceptualization. **Rongze Tang:** Formal analysis, Data

curation, Conceptualization. **Silin Du**: Formal analysis, Data curation, Conceptualization. **Yingcai Xu**: Data curation, Conceptualization. **Jiangbo Wang**: Visualization, Validation, Supervision. **Fenglei Gao**: Visualization, Validation, Supervision. **Guanqun Zhang**: Visualization, Validation, Supervision.

Declaration of competing interest

The authors declare that they have no known competing financial interests or personal relationships that could have appeared to influence the work reported in this paper.

Acknowledgements

The authors gratefully acknowledge financial support from the Graduate Research and Innovation Projects of Jiangsu Province (KYCX24_3122) and the QingLan Research Project of Jiangsu Province. The studies detailed in this article were conducted at the Xuzhou Medical University Public Experimental Research Center. Additionally, gratitude is expressed to Figdraw for creating [Scheme 1](#).

Appendix A. Supplementary data

Supplementary data to this article can be found online at <https://doi.org/10.1016/j.cej.2026.173795>.

Data availability

Data will be made available on request.

References

- W. Liu, W. Deng, X. Gong, J. Ou, S. Yu, S. Chen, Global burden of Alzheimer's disease and other dementias in adults aged 65 years and over, and health inequality related to SDI, 1990–2021: analysis of data from GBD 2021, *BMC Public Health* 25 (1) (2025) 1256, <https://doi.org/10.1186/s12889-025-22378-z>.
- J. Zhang, Y. Zhang, J. Wang, Y. Xia, J. Zhang, L. Chen, Recent advances in Alzheimer's disease: mechanisms, clinical trials and new drug development strategies, *Signal Transduct. Target. Ther.* 9 (1) (2024) 211, <https://doi.org/10.1038/s41392-024-01911-3>.
- G. Pfundstein, A.G. Nikonenko, V. Sytnyk, Amyloid precursor protein (APP) and amyloid β (A β) interact with cell adhesion molecules: implications in Alzheimer's disease and normal physiology, *Front. Cell Dev. Biol.* 10 (2022) 969547, <https://doi.org/10.3389/fcell.2022.969547>.
- P. Goel, S. Chakrabarti, K. Goel, K. Bhutani, T. Chopra, S. Bali, Neuronal cell death mechanisms in Alzheimer's disease: an insight, *Front. Mol. Neurosci.* 15 (2022) 937133, <https://doi.org/10.3389/fnmol.2022.937133>.
- T. Ma, J. Du, Y. Zhang, B. Wang, T. Zhang, GPX4-independent ferroptosis: a new strategy in disease's therapy, *Cell Death Discov.* 8 (1) (2022) 434, <https://doi.org/10.1038/s41420-022-01212-0>.
- L. Tan, J. Xie, C. Liao, X. Li, W. Zhang, C. Cai, L. Cheng, X. Wang, Tetrahedral framework nucleic acids inhibit A β -mediated ferroptosis and ameliorate cognitive and synaptic impairments in Alzheimer's disease, *J. Nanobiotechnol.* 22 (1) (2024) 682, <https://doi.org/10.1186/s12951-024-02963-x>.
- Y. Zhang, M. Wang, W. Chang, Iron dyshomeostasis and ferroptosis in Alzheimer's disease: molecular mechanisms of cell death and novel therapeutic drugs and targets for AD, *Front. Pharmacol.* 13 (2022) 983623, <https://doi.org/10.3389/fphar.2022.983623>.
- X.X. Qu, J.H. He, Z.Q. Cui, T. Yang, X.H. Sun, PPAR- α agonist GW7647 protects against oxidative stress and iron deposit via GPx4 in a transgenic mouse model of Alzheimer's diseases, *ACS Chem. Neurosci.* 13 (2) (2022) 207–216, <https://doi.org/10.1021/acscchemneuro.1c00516>.
- M. Dahiya, A. Kumar, M. Yadav, S. Chauhan, β -Pinene ameliorates ICV-STZ induced Alzheimer's pathology via antioxidant, anticholinesterase, and mitochondrial protective effects: in-silico and in-vivo studies, *Eur. J. Pharmacol.* 991 (2025) 177307, <https://doi.org/10.1016/j.ejphar.2025.177307>.
- J. Wang, Z. Wang, Y. Li, Y. Hou, C. Yin, E. Yang, Z. Liao, C. Fan, L.L. Martin, D. Sun, Blood brain barrier-targeted delivery of double selenium nanospheres ameliorates neural ferroptosis in Alzheimer's disease, *Biomaterials* 302 (2023) 122359, <https://doi.org/10.1016/j.biomaterials.2023.122359>.
- C. Sangokoya, The FIRE biosensor illuminates iron regulatory protein activity and cellular iron homeostasis, *Cell Rep Methods* 5 (1) (2025) 100960, <https://doi.org/10.1016/j.crmeth.2024.100960>.
- I. Yanatori, D.R. Richardson, K. Imada, F. Kishi, Iron export through the transporter Ferroportin 1 is modulated by the Iron chaperone PCBP2, *J. Biol. Chem.* 291 (33) (2016) 17303–17318, <https://doi.org/10.1074/jbc.M116.721936>.
- D.L. Zhang, M.C. Ghosh, T.A. Rouault, The physiological functions of iron regulatory proteins in iron homeostasis - an update, *Front. Pharmacol.* 5 (2014) 124, <https://doi.org/10.3389/fphar.2014.00124>.
- H. Moorthy, M. Ramesh, D. Padhi, P. Baruah, T. Govindaraju, Polycatechols inhibit ferroptosis and modulate tau liquid-liquid phase separation to mitigate Alzheimer's disease, *Mater. Horiz.* 11 (13) (2024) 3082–3089, <https://doi.org/10.1039/d4mh00023d>.
- T. Nakamura, I. Naguro, H. Ichijo, Iron homeostasis and iron-regulated ROS in cell death, senescence and human diseases, *Biochim. Biophys. Acta Gen. Subj.* 1863 (9) (2019) 1398–1409, <https://doi.org/10.1016/j.bbagen.2019.06.010>.
- R.L. Bertrand, Iron accumulation, glutathione depletion, and lipid peroxidation must occur simultaneously during ferroptosis and are mutually amplifying events, *Med. Hypotheses* 101 (2017) 69–74, <https://doi.org/10.1016/j.mehy.2017.02.017>.
- Q. Mu, L. Chen, X. Gao, S. Shen, W. Sheng, J. Min, F. Wang, The role of iron homeostasis in remodeling immune function and regulating inflammatory disease, *Sci Bull (Beijing)* 66 (17) (2021) 1806–1816, <https://doi.org/10.1016/j.scib.2021.02.010>.
- J. Kumar, A. Varela-Ramirez, M. Narayan, Development of novel carbon-based biomedical platforms for intervention in xenotoxicant-induced Parkinson's disease onset, *BMEat* 2 (4) (2024) e12072, <https://doi.org/10.1002/bmm2.12072>.
- H. Long, W. Zhu, L. Wei, J. Zhao, Iron homeostasis imbalance and ferroptosis in brain diseases, *MedComm* 4 (4) (2023), <https://doi.org/10.1002/mco2.298> (2020) e298.
- Y. Li, Y. Duan, Y. Li, Y. Gu, L. Zhou, Z. Xiao, X. Yu, Y. Cai, E. Cheng, Q. Liu, Y. Jiang, Q. Yang, F. Zhang, Q. Lei, B. Yang, Cascade loop of ferroptosis induction and immunotherapy based on metal-phenolic networks for combined therapy of colorectal cancer, *Exploration (Beijing, China)* 5 (1) (2024) 20230117, <https://doi.org/10.1002/EXP.20230117>.
- Y. Jiang, N. Krishnan, J. Heo, R.H. Fang, L. Zhang, Nanoparticle-hydrogel superstructures for biomedical applications, *J. Control. Release* 324 (2020) 505–521, <https://doi.org/10.1016/j.jconrel.2020.05.041>.
- Z. Ahmadian, F. Kazeminava, M. Afrouz, M. Abbaszadeh, N.T. Mehr, J.A. Shiran, C. Gouda, M. Adeli, H.S. Kafil, A review on the impacts of metal/metal nanoparticles on characteristics of hydrogels: special focus on carbohydrate polymers, *Int. J. Biol. Macromol.* 253 (Pt 1) (2023) 126535, <https://doi.org/10.1016/j.ijbiomac.2023.126535>.
- F. Veider, E. Sanchez Armengol, A. Bernkop-Schnürch, Charge-reversible nanoparticles: advanced delivery Systems for Therapy and Diagnosis, *Small* 20 (3) (2024) e2304713, <https://doi.org/10.1002/sml.202304713>.
- Q. Truong Hoang, K.A. Huynh, T.G. Nguyen Cao, J.H. Kang, X.N. Dang, V. Ravichandran, H.C. Kang, M. Lee, J.E. Kim, Y.T. Ko, T.I. Lee, M.S. Shim, Piezocatalytic 2D WS(2) Nanosheets for ultrasound-triggered and mitochondria-targeted Piezodynamic Cancer therapy synergized with energy metabolism-targeted chemotherapy, *Adv. Mater.* 35 (18) (2023) e2300437, <https://doi.org/10.1002/adma.202300437>.
- L. Zhang, M. Feng, X. Wang, H. Zhang, J. Ding, Z. Cheng, L. Qian, Peptide Szeto-schiller 31 ameliorates doxorubicin-induced cardiotoxicity by inhibiting the activation of the p38 MAPK signaling pathway, *Int. J. Mol. Med.* 47 (4) (2021), <https://doi.org/10.3892/ijmm.2021.4896>.
- H. Wang, B. Fang, B. Peng, L. Wang, Y. Xue, H. Bai, S. Lu, N.H. Voelcker, L. Li, L. Fu, W. Huang, Recent advances in chemical biology of mitochondria targeting, *Front. Chem.* 9 (2021) 683220, <https://doi.org/10.3389/fchem.2021.683220>.
- L. Deng, Y. Qi, Z. Liu, Y. Xi, W. Xue, Effect of tannic acid on blood components and functions, *Colloids Surf. B Biointerfaces* 184 (2019) 110505, <https://doi.org/10.1016/j.colsurfb.2019.110505>.
- H. Jafari, P. Ghaffari-Bohlouli, S.V. Niknezhad, A. Abedi, Z. Izadifar, R. Mohammadnejad, R.S. Varma, A. Shavandi, Tannic acid: a versatile polyphenol for design of biomedical hydrogels, *J. Mater. Chem. B* 10 (31) (2022) 5873–5912, <https://doi.org/10.1039/d2tb01056a>.
- M. Heidarzadeh, Y. Gürsoy-Özdemir, M. Kaya, A. Eslami Abriz, A. Zarebkohan, R. Rahbarghazi, E. Sokullu, Exosomal delivery of therapeutic modulators through the blood-brain barrier: promise and pitfalls, *Cell Biosci.* 11 (1) (2021) 142, <https://doi.org/10.1186/s13578-021-00650-0>.
- K. Xie, Y. Mo, E. Yue, N. Shi, K. Liu, Exosomes derived from M2-type microglia ameliorate oxygen-glucose deprivation/reoxygenation-induced HT22 cell injury by regulating miR-124-3p/NCOA4-mediated ferroptosis, *Heliyon* 9 (7) (2023) e17592, <https://doi.org/10.1016/j.heliyon.2023.e17592>.
- G.E. Arteel, H. Sies, The biochemistry of selenium and the glutathione system, *Environ. Toxicol. Pharmacol.* 10 (4) (2001) 153–158, [https://doi.org/10.1016/s1382-6689\(01\)00078-3](https://doi.org/10.1016/s1382-6689(01)00078-3).
- K. Weaver, R. Skouta, The Selenoprotein glutathione peroxidase 4: from molecular mechanisms to novel therapeutic opportunities, *Biomedicines* 10 (4) (2022), <https://doi.org/10.3390/biomedicines10040891>.
- Z. Miao, S. Jiang, M. Ding, S. Sun, Y. Ma, M.R. Younis, G. He, J. Wang, J. Lin, Z. Cao, P. Huang, Z. Zha, Ultrasmall rhodium Nanozyme with RONS scavenging and Photothermal activities for anti-inflammation and antitumor Theranostics of Colon diseases, *Nano Lett.* 20 (5) (2020) 3079–3089, <https://doi.org/10.1021/acs.nanolett.9b05035>.
- J. Gao, Q. Song, G. Gu, G. Jiang, J. Huang, Y. Tang, R. Yu, A. Wang, Y. Huang, G. Zheng, H. Chen, X. Gao, Intracerebral fate of organic and inorganic nanoparticles is dependent on microglial extracellular vesicle function, *Nat. Nanotechnol.* 19 (3) (2024) 376–386, <https://doi.org/10.1038/s41565-023-01551-8>.
- N. Takahashi, P. Cho, L.M. Selfors, H.J. Kuiken, R. Kaul, T. Fujiwara, I.S. Harris, T. Zhang, S.P. Gygi, J.S. Brugge, 3D culture models with CRISPR screens reveal

- hyperactive NRF2 as a prerequisite for spheroid formation via regulation of proliferation and Ferroptosis, *Mol. Cell* 80 (5) (2020) 828–844.e6, <https://doi.org/10.1016/j.molcel.2020.10.010>.
- [36] X. Chen, Z. Zhong, Z. Xu, L. Chen, Y. Wang, 2',7'-Dichlorodihydrofluorescein as a fluorescent probe for reactive oxygen species measurement: forty years of application and controversy, *Free Radic. Res.* 44 (6) (2010) 587–604, <https://doi.org/10.3109/10715761003709802>.
- [37] D.J. Lane, A.M. Merlot, M.L. Huang, D.H. Bae, P.J. Jansson, S. Sahni, D. S. Kalinowski, D.R. Richardson, Cellular iron uptake, trafficking and metabolism: key molecules and mechanisms and their roles in disease, *Biochim. Biophys. Acta* 1853 (5) (2015) 1130–1144, <https://doi.org/10.1016/j.bbamer.2015.01.021>.
- [38] J. Wang, P. Shangguan, X. Chen, Y. Zhong, M. Lin, M. He, Y. Liu, Y. Zhou, X. Pang, L. Han, M. Lu, X. Wang, Y. Liu, H. Yang, J. Chen, C. Song, J. Zhang, X. Wang, B. Shi, B.Z. Tang, A one-two punch targeting reactive oxygen species and fibril for rescuing Alzheimer's disease, *Nat. Commun.* 15 (1) (2024) 705, <https://doi.org/10.1038/s41467-024-44737-x>.
- [39] B. Kabiş, E. Gürses, A. Işıkay, S. Aksoy, Spatial memory and learning: investigating the role of dynamic visual acuity, *Front. Behav. Neurosci.* 18 (2024) 1429069, <https://doi.org/10.3389/fnbeh.2024.1429069>.
- [40] S.S. Zhao, W.N. Yang, H. Jin, K.G. Ma, G.F. Feng, Puerarin attenuates learning and memory impairments and inhibits oxidative stress in STZ-induced SAD mice, *Neurotoxicology* 51 (2015) 166–171, <https://doi.org/10.1016/j.neuro.2015.10.010>.
- [41] A.K. Kraeuter, P.C. Guest, Z. Sarnyai, The Y-maze for assessment of spatial working and reference memory in mice, *Methods Mol. Biol.* 1916 (2019) 105–111, https://doi.org/10.1007/978-1-4939-8994-2_10.
- [42] M.J. Ko, G.E. Mulia, R.M. van Rijn, Commonly used anesthesia/euthanasia methods for brain collection differentially impact MAPK activity in male and female C57BL/6 mice, *Front. Cell. Neurosci.* 13 (2019) 96, <https://doi.org/10.3389/fncel.2019.00096>.
- [43] V. Bitonto, F. Garelli, A. Scherberich, M. Filippi, Prussian blue staining to visualize Iron oxide nanoparticles, *Methods Mol. Biol.* 2566 (2023) 321–332, https://doi.org/10.1007/978-1-0716-2675-7_26.
- [44] N.K. Mondal, H. Saha, B. Mukherjee, N. Tyagi, M.R. Ray, Inflammation, oxidative stress, and higher expression levels of Nrf2 and NQO1 proteins in the airways of women chronically exposed to biomass fuel smoke, *Mol. Cell. Biochem.* 447 (1–2) (2018) 63–76, <https://doi.org/10.1007/s11010-018-3293-0>.
- [45] Q. Ru, Y. Li, L. Chen, Y. Wu, J. Min, F. Wang, Iron homeostasis and ferroptosis in human diseases: mechanisms and therapeutic prospects, *Signal Transduct. Target. Ther.* 9 (1) (2024) 271, <https://doi.org/10.1038/s41392-024-01969-z>.
- [46] S. Samanta, F. Akhter, A. Roy, D. Chen, B. Turner, Y. Wang, N. Clemente, C. Wang, R.H. Swerdlow, K.P. Battaile, S. Lovell, S.F. Yan, S.S. Yan, New cyclophilin D inhibitor rescues mitochondrial and cognitive function in Alzheimer's disease, *Brain* 147 (5) (2024) 1710–1725, <https://doi.org/10.1093/brain/awad432>.